JWST+ALMA Reveal the Interstellar Medium Kinematics and Stellar Structure of MAMBO-9, a Merging Pair of DSFGs in an Overdense

Citation for the original published paper (version of record):
Akins, H., Casey, C., Champagne, J. et al (2026). JWST+ALMA Reveal the Interstellar Medium Kinematics and Stellar Structure of MAMBO-9, a Merging
Pair of DSFGs in an Overdense Environment at z = 5.85. Astrophysical Journal, 1006(2).
http://dx.doi.org/10.3847/1538-4357/ae8449

The Astrophysical Journal, 1006:229 (15pp), 2026 August 1 https://doi.org/10.3847/1538-4357/ae8449

JWST+ALMA Reveal the Interstellar Medium Kinematics and Stellar Structure of MAMBO-9, a Merging Pair of DSFGs in an Overdense Environment at $z = 5.85$

Hollis B. Akins[1,16], Caitlin M. Casey[1,2,3], Jaclyn B. Champagne[4], Olivia Cooper[5,16,17], Maximilien Franco[6], Seiji Fujimoto[1,7,8,18], Kirsten K. Knudsen[9], Anton M. Koekemoer[10], Arianna S. Long[11], Allison Man[12], Sinclaire M. Manning[13,18], Jed McKinney[1,18], Jorge Zavala[13], Pablo Arrabal Haro[14], Mark Dickinson[15], Vasily Kokorev[1], and Anthony J. Taylor[1]

[1] Department of Astronomy, The University of Texas at Austin, 2515 Speedway Blvd Stop C1400, Austin, TX 78712, USA; hollis.akins@gmail.com
[2] Department of Physics, University of California, Santa Barbara, CA 93106, USA
[3] Cosmic Dawn Center (DAWN), Denmark
[4] Steward Observatory, University of Arizona, 933 N Cherry Ave, Tucson, AZ 85721, USA
[5] Department for Astrophysical and Planetary Science, University of Colorado, Boulder, CO 80309, USA
[6] Université Paris-Saclay, Université Paris Cité, CEA, CNRS, AIM, 91191, Gif-sur-Yvette, France
[7] David A. Dunlap Department of Astronomy and Astrophysics, University of Toronto, 50 St. George Street, Toronto, Ontario, M5S 3H4, Canada
[8] Dunlap Institute for Astronomy and Astrophysics, University of Toronto, 50 St. George Street, Toronto, Ontario, M5S 3H4, Canada
[9] Department of Space, Earth and Environment, Chalmers University of Technology, SE-412 96 Gothenburg, Sweden
[10] Space Telescope Science Institute, 3700 San Martin Drive, Baltimore, MD 21218, USA
[11] Department of Astronomy, The University of Washington, Seattle, WA 98195, USA
[12] Department of Physics & Astronomy, University of British Columbia, 6224 Agricultural Road, Vancouver, BC V6T 1Z1, Canada
[13] Department of Astronomy, University of Massachusetts Amherst, 710 N Pleasant Street, Amherst, MA 01003, USA
[14] Astrophysics Science Division, NASA Goddard Space Flight Center, 8800 Greenbelt Rd, Greenbelt, MD 20771, USA
[15] NSF's National Optical-Infrared Astronomy Research Laboratory, 950 N. Cherry Ave., Tucson, AZ 85719, USA
Received 2025 August 8; revised 2026 June 8; accepted 2026 June 12; published 2026 July 29

Abstract

We present high-resolution Atacama Large Millimeter/submillimeter Array (ALMA) [C II] 158 μm observations and JWST/NIRCam+MIRI imaging of MAMBO-9, a pair of optically dark, dusty star-forming galaxies at $z = 5.85$. MAMBO-9 is among the most massive, gas-rich, and actively star-forming galaxies at this epoch, when the Universe was less than 1 Gyr old. The new 400 pc resolution [C II] observations reveal velocity gradients in both objects; we estimate the dynamical masses and find a relative mass ratio of 1:5. The kinematics of both objects suggest both rotation and strong tidal interaction, suggesting that the pair has already experienced a close encounter. Indeed, the new JWST imaging reveals a continuous bridge of moderately dust-obscured material between the two. We perform spatially resolved spectral energy distribution (SED) fitting using the high-resolution ALMA+JWST imaging, finding that the majority of the recent star formation is concentrated in extremely obscured ($A_V > 10$) clouds, while the majority of the rest-optical light (stellar continuum and Hα emission) is emergent from moderately to highly obscured ($A_V \sim$ 1–5) regions on the outskirts. Combining our new stellar and dynamical mass measurements with previous CO observations, we find that the mass budget of MAMBO-9 requires a CO-to-H_2 conversion factor (α_{CO}) of order unity ($\sim$1–2), indicative of a highly metal-enriched interstellar medium. Finally, we show that MAMBO-9 resides in a large overdensity spanning the PRIMER-COSMOS field, with 39 galaxies spectroscopically confirmed within $\sim$25 cMpc. With a total baryonic mass of $\sim 10^{11}\,M_\odot$, MAMBO-9 can be considered a prototype of massive galaxy formation and a likely progenitor of the brightest cluster galaxies in the lower-redshift Universe.

Unified Astronomy Thesaurus concepts: Galaxy evolution (594); Galaxy formation (595); High-redshift galaxies (734); Interstellar medium (847); Circumgalactic medium (1879)

1. Introduction

The first 3 Gyr of the Universe, from the end of reionization around $z \sim 6$ to cosmic noon at $z \sim 2$, marks an era of extraordinary galaxy growth and rapid stellar mass assembly (P. Madau & M. Dickinson 2014). Much of that growth, however, is obscured by dust; the most intensely star-forming galaxies at $z \gtrsim 2$, the submillimeter galaxies (SMGs; D. H. Hughes et al. 1998; A. W. Blain et al. 2002) or dusty star-forming galaxies (DSFGs; C. M. Casey et al. 2014), represent the dominant contributor to the obscured star formation rate density (SFRD). To higher redshifts, $z \sim$ 3–6, these objects can be completely obscured at optical and near-IR (NIR) wavelengths (e.g., F. Walter et al. 2012; D. A. Riechers et al. 2013; D. P. Marrone et al. 2018; C. M. Casey et al. 2019; T. Wang et al. 2019; C. C. Williams et al. 2019; M. Talia et al. 2021; S. M. Manning et al. 2022) and may constitute some $\sim$20%–50% of the SFRD, which is entirely missed by surveys targeting only the rest-frame UV (J. A. Zavala et al. 2021; H. S. B. Algera et al. 2023; S. Fujimoto et al. 2023).

The population of DSFGs in the early Universe has been elusive. Their high obscuration at rest-UV and optical wavelengths has prohibited characterization optical/NIR surveys, and the strong redshift degeneracies with DSFGs at lower redshift

[16] NSF Graduate Research Fellow.
[17] NSF Astronomy & Astrophysics Postdoctoral Fellow.
[18] Hubble Fellow.

(which are ∼20–100 times more numerous; e.g., V. Smolčić et al. 2012) has made submillimeter selection challenging. Much progress has been made on this front in recent years by focusing on gravitationally lensed objects (D. P. Marrone et al. 2018; J. A. Zavala et al. 2018a; F. Sun et al. 2024) or observing at longer wavelengths (e.g., 2–3 mm) to efficiently filter out lower-redshift galaxies (e.g., C. C. Williams et al. 2019; C. M. Casey et al. 2021; J. A. Zavala et al. 2021; O. R. Cooper et al. 2022).

Moreover, far-IR (FIR) emission lines have proven effective tools for redshift confirmation and characterization of high-z DSFGs. Atacama Large Millimeter/submillimeter Array (ALMA) spectral line scans have confirmed numerous $z > 3$ SMGs via multiple CO and [C I] detections (C.-C. Chen et al. 2022). At $z \gtrsim 5$, the FIR fine-structure lines of [C II] 158 μm and [O III] 88 μm (among others) fall into the submillimeter/millimeter range. The [C II] 158 μm line in particular is one of the brightest FIR lines, as its low ionization potential (11.26 eV) makes it a dominant coolant of the neutral interstellar medium (ISM). As such, it has served as a powerful tool for measuring spectroscopic redshifts (e.g., Y. Fudamoto et al. 2021; R. J. Bouwens et al. 2022; S. Schouws et al. 2023), gas kinematics (e.g., R. Wang et al. 2013; R. Smit et al. 2018; M. Kohandel et al. 2019; G. C. Jones et al. 2021; L. E. Rowland et al. 2024), and ISM properties (e.g., Y. Harikane et al. 2020; K. C. Litke et al. 2022, 2023; M. Killi et al. 2023). Importantly, observations of bright FIR lines like [C II] have made possible reliable dynamical mass measurements, even in heavily obscured systems (e.g., F. Rizzo et al. 2021). Regardless, the stellar properties of DSFGs have remained poorly constrained, limiting our ability to place these objects in context in early galaxy evolution.

The launch of the James Webb Space Telescope (JWST) has opened up our view into the rest-frame optical and NIR for $z \gtrsim 4$ galaxies. Already, JWST has brought about the first rest-frame optical detections of numerous galaxies previously only detected in the submillimeter (e.g., J. McKinney et al. 2023; J. A. Zavala et al. 2023; F. Gentile et al. 2024; F. Sun et al. 2024; M. Xiao et al. 2024; J. A. Hodge et al. 2025), as well as the identification of previously unknown "Hubble Space Telescope (HST)–dark" massive galaxy candidates at $z \gtrsim 4$ (e.g., L. Barrufet et al. 2023, 2025; K. Chworowsky et al. 2024; E. Nelson et al. 2024; C. C. Williams et al. 2024). The high spatial resolution and incredible sensitivity of JWST has also facilitated spatially resolved analysis, even in heavily dust-obscured objects (e.g., L. Colina et al. 2023; V. Kokorev et al. 2023; P. G. Pérez-González et al. 2023; A. Crespo Gómez et al. 2024; P. S. Kamieneski et al. 2024; G. Rodighiero et al. 2024; G. C. Jones et al. 2025). These works have generally revealed significant substructure, with strong gradients in stellar and ISM properties across individual galaxies, implying a complex assembly history driven by multiple separate star formation episodes and/or mergers.

This paper presents high-resolution ALMA and JWST observations of MAMBO-9—a pair of massive DSFGs at $z = 5.85$. MAMBO-9 was first identified by F. Bertoldi et al. (2007) with the MAMBO instrument on the Institut de Radioastronomie Millimétrique (IRAM) 30 m telescope, and later corroborated with AzTEC and SCUBA-2 detections (I. Aretxaga et al. 2011; C. M. Casey et al. 2013). MAMBO-9 was identified as a potentially high-z DSFG based on nondetections in Herschel imaging at 100–500 μm, and its redshift was confirmed at $z = 5.850$ by S. Jin et al. (2019) and C. M. Casey et al. (2019), based on the detection of the ^{12}CO($J = 6 \rightarrow 5$) and $H_2O(2_{1,1}–2_{0,2})$ lines. Among the highest-redshift DSFGs known, MAMBO-9 provides unique insight into the extremes of galaxy formation in the early Universe.

Here, we use new high-resolution (∼400 pc) ALMA [C II] 158 μm and dust continuum observations, in conjunction with JWST/NIRCam+MIRI imaging, to constrain MAMBO-9's stellar/ISM properties and kinematics. In Section 2, we describe the ALMA and JWST observations and data reduction. In Section 3, we describe our main results. The the ALMA [C II] and dust continuum measurements (Section 3.1) provide kinematics and constraints on the dynamical mass (Section 3.2), while the JWST imaging (Section 3.3) allows the derivation of stellar masses from spectral energy distribution (SED) fitting (Section 3.5). In Section 4, we discuss our results—in particular, the baryonic mass budget (Section 4.2) and environment of MAMBO-9 (Section 4.3). Throughout this work, we adopt a P. Kroupa (2002) stellar initial mass function (IMF) and a cosmology consistent with the Planck Collaboration et al. (2020) results ($H_0 = 67.66$ km s^{-1} Mpc^{-1}, $\Omega_{m,0} = 0.31$). All magnitudes are quoted in the AB system (J. B. Oke 1974).

2. Data and Observations

2.1. ALMA Data

We used ALMA observations of MAMBO-9 (R.A. $10^h00^m26\overset{s}{.}358$, decl. $+02^\circ\ 15'\ 27\overset{''}{.}923$) in Band 7 from ALMA program ID #2021.1.00505.S (PI: C. Casey). Based on the spectroscopic redshift of $z = 5.85$ (C. M. Casey et al. 2019), the Band 7 observations were tuned to cover the [C II] 158 μm line; spectral windows were tuned to cover 276.48–278.46, 278.44–280.42, 288.48–290.46, and 290.48–292.46 GHz. Observations were carried out in the C9 configuration, yielding a nominal beam size of $\sim 0\overset{''}{.}05$ and a maximum recoverable scale (MRS) of $\sim 0\overset{''}{.}25$.

The reduction and imaging of the ALMA data were performed with the Common Astronomy Software Applications (CASA) package (J. P. McMullin et al. 2007), version 6.5.2, following the standard ALMA pipeline reduction scripts. We additionally identified and flagged a few noisy channels (due to an atmospheric line at $\nu_{\rm obs} \sim 289$ GHz) in one of the continuum spectral windows. All images were produced with the `tclean` task in CASA, using natural weighting to maximize the sensitivity for any spatially extended emission, given the small MRS of our data. Cleaning was performed using the "auto-multithresh" automasking algorithm (A. A. Kepley et al. 2020), with the parameters recommended in the CASA documentation, and the "multiscale" deconvolver (T. J. Cornwell 2008), with scales of 0 (delta function) and 1 times the beam size. The continuum map was produced using the multi-frequency synthesis (`mfs`; J. E. Conway et al. 1990) mode in CASA, masking channels $\leqslant 1000$ km s^{-1} away from the expected line center. A continuum-subtracted measurement set was produced with the `uvcontsub` task in CASA, measuring the continuum in the same frequency range with a fit order of 1. The [C II] data cube was then produced from this continuum-subtracted measurement set.

For the continuum map, we obtain an rms of 14 μJy beam^{-1}. For the [C II] data cube, we obtain an rms of 0.14 mJy beam^{-1} per 20 km s^{-1} channel. All measurements are done on primary-beam-corrected maps; we generate an rms map by computing the rms before this correction and weighting by the primary beam. MAMBO-9-A sits at the phase center. With natural weighting, the synthesized beam size is 0.″07 × 0.″06, which corresponds to a physical resolution (FWHM) of ∼400 pc.

2.2. JWST Data

In addition to the high-resolution ALMA data presented in this work, we utilize recent JWST/NIRCam observations taken as part of the Public Release IMaging for Extragalactic Research (PRIMER) survey (GO#1837; PI: J. Dunlop; see also C. T. Donnan et al. 2024). PRIMER is a large Cycle 1 Treasury Program to image the UDS and COSMOS legacy fields in CANDELS (N. A. Grogin et al. 2011; A. M. Koekemoer et al. 2011) with NIRCam+MIRI. The PRIMER imaging includes eight NIRCam bands (F090W, F115W, F150W, F200W, F277W, F356W, F410M, and F444W), plus two MIRI bands (F770W and F1800W).

NIRCam observations covering MAMBO-9 were taken in 2023 April, and MIRI observations were taken in 2023 November. The raw NIRCam imaging was reduced by the JWST Calibration Pipeline, version 1.12.1 (H. Bushouse et al. 2023),[19] with the addition of several custom modifications (as has also been done for other JWST studies; e.g., M. B. Bagley et al. 2023), including the subtraction of $1/f$ noise and sky background. We use the Calibration Reference Data System (CRDS) pmap 1170, which corresponds to NIRCam instrument mapping imap 0273. The MIRI/F770W observations were reduced using version 1.12.5 of the JWST Calibration pipeline, along with additional steps for background subtraction, which was necessary to mitigate instrumental effects. The mosaics in all 10 NIRCam+MIRI bands are produced at a pixel scale of 0.″03 pix^{-1} and astrometrically aligned to a reference catalog from HST F814W imaging of the field (A. M. Koekemoer et al. 2007), which is itself aligned to Gaia (Gaia Collaboration et al. 2018). The astrometric accuracy is estimated to be <5 (10) mas for NIRCam (MIRI). The NIRCam and MIRI imaging reduction follows the methods used for the COSMOS-Web survey (see S. Harish et al. 2025; M. Franco et al. 2026).

Throughout this work, we measure photometry for MAMBO-9 by summing the flux within custom apertures defined on point-spread function (PSF)–homogenized images. However, the pipeline-produced error maps treat pixels as independent, underestimating the true uncertainty in practice, due to correlated noise. We therefore estimate photometric uncertainties empirically, using random apertures. In each band, we place ∼4000 circular apertures at random, source-free positions in the vicinity of MAMBO-9, spanning a range of aperture sizes, and measure the scatter in the enclosed flux as a function of the aperture area $N_{\rm pix}$. We fit the resulting $\sigma(N_{\rm pix})$ relation and adopt this calibration for all photometric uncertainties reported and used in SED fitting.

We additionally make use of recent JWST/NIRSpec observations from the program CANDELS Area PRISM Epoch of Reionization Survey (CAPERS; GO#6368; PI: M. Dickinson). CAPERS is a JWST Cycle 3 Treasury program using the NIRSpec MSA with the PRISM to observe very-high-redshift galaxies, active galactic nucleus (AGN) candidates, and other objects of community interest in three of the CANDELS legacy fields (N. A. Grogin et al. 2011; A. M. Koekemoer et al. 2011). The PRISM disperser covers 0.6–5.3 μm at low resolution ($R \sim 100$). CAPERS observed seven pointings in the PRIMER-COSMOS field, each with three separate MSA configurations; high-priority targets were observed in multiple configurations, while lower-priority targets were observed in only one or two, to maximize the total spectroscopic yield. MAMBO-9 was selected for follow-up given its high redshift relative to the full SMG population, and MAMBO-9-B received the full 4.74 hr of exposure (MAMBO-9-A was not observed). Details of the NIRSpec data reduction and optimal extraction are provided in A. J. Taylor et al. (2025) and C. T. Donnan et al. (2025). We additionally make use of JWST/NIRSpec observations of sources in the field from two further programs—DD#6585 (PI: D. Coulter) and GO#1810 (PI: S. Belli)—in our overdensity analysis (Section 4.3); these data were reduced following the same procedure as the CAPERS observations described above.

[19] https://github.com/spacetelescope/jwst

3. Results

3.1. High-resolution ALMA [C II] Line and Dust Continuum Measurements

Figure 1 shows both the high-resolution [C II] 158 μm and dust continuum measurements for the MAMBO-9 system. The dust continuum map and [C II] 158 μm moment 0 map are shown in the left panels, with contours following a Fibonacci sequence (-3σ, 3σ, 5σ, 8σ, 13σ, 21σ, and 34σ). The [C II] moment 0 map is integrated from −500 to +500 km s^{-1} relative to the line center at 277.45 GHz. The right panels show the [C II] line spectra for the two galaxies with single- and double-Gaussian fits applied. The spectra and [C II] flux measurements are extracted from regions within the $>1.5\sigma$ contour on the [C II] moment 0 map, shown with the gray dashed contours in Figure 1.

MAMBO-9-A is detected at a peak signal-to-noise ratio (SNR) of ∼50 in the dust continuum map and shows a spheroidal/symmetric morphology consistent with previous dust continuum observations (C. M. Casey et al. 2019). MAMBO-9-B is detected at a peak SNR ∼13 in dust continuum in its southwest core, with a prominent tail extending toward the northeast. This extended tail is also seen in the [C II] moment 0 map, though the [C II] emission is more diffuse. The peak position of the [C II] emission in MAMBO-9-A is offset from the peak continuum position, suggesting some decoupling of the [C II]- and IR-emitting gas.

The [C II] spectrum for MAMBO-9-A shows a double-peaked line profile, separated by ≈500 km s^{-1}, consistent with the spectrum for ^{12}CO($J = 6 \rightarrow 5$) presented in C. M. Casey et al. (2019). We fit the spectrum to both single- and double-Gaussian models; the latter is a significant improvement over the former, with a reduced chi-squared of $\chi^2_\nu = 1.05$ versus 1.71. The double-peaked emission-line spectrum is consistent with strong rotation (see Section 3.2), and is also seen in MAMBO-9-B, albeit with a smaller separation, suggesting a lower dynamical mass. MAMBO-9-B also shows a possible third peak at a velocity of ∼−450 km s^{-1}; however, adding a third Gaussian component does not substantially reduce the χ^2_ν.

The integrated [C II] luminosities for MAMBO-9-A and B are $L_{\rm [C\,II]}$ =(3.1 ± 0.2) × 10^9 $L_\odot$ and (3.3 ± 0.3) × 10^9 $L_\odot$, respectively. These luminosities are roughly equal, despite

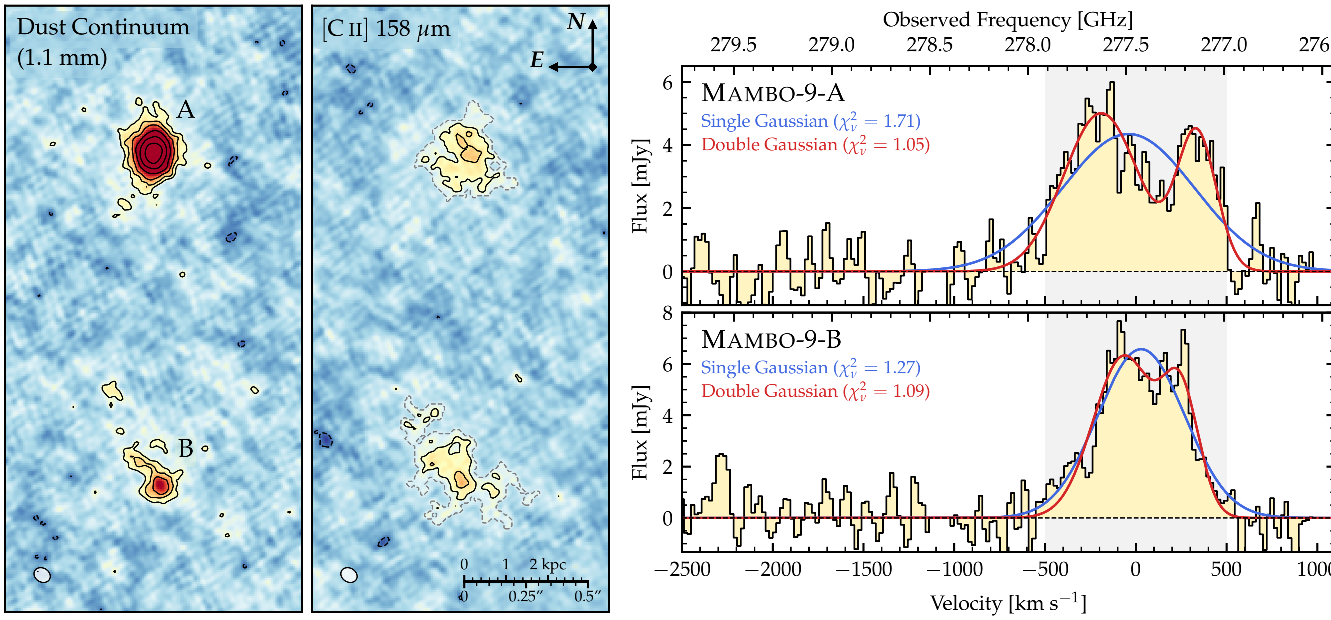

Figure 1. Left: ALMA dust continuum and [C II] 158 μm moment 0 maps for the MAMBO-9 system. The contours indicate the significance level, starting from -3σ, 3σ and increasing following a Fibonacci sequence thereafter. The [C II] moment 0 map is integrated from $-500 \leqslant v$ km s$^{-2} \leqslant 500$. The gray dashed contours indicate the segmentation map that is used to extract spectra. Right: [C II] line spectra for both MAMBO-9-A and B, with Gaussian and double-Gaussian fits applied. For both objects, the double-Gaussian fit is a significant improvement over the single Gaussian, based on the reduced χ^2 statistic. The double-peaked [C II] spectra are suggestive of strong rotation, and the dust continuum and [C II] maps suggest a disturbed morphology due to the galaxy interaction.

MAMBO-9-A being a factor of ~3.5 brighter in the continuum. Using the I. De Looze et al. (2014) calibration for H II/starburst galaxies, these luminosities would correspond to SFRs of SFR$_{\rm [C\,II]}$ = 270 ± 190 and 290 ± 200 $M_\odot$ yr^{-1} for MAMBO-9-A and B, respectively. These SFRs are underestimated relative to the FIR continuum-derived SFRs (C. M. Casey et al. 2019), which may be due to the "[C II] deficit"—a known phenomenon in which [C II] emission is reduced in intensely star-forming galaxies. Figure 2 shows the $L_{\rm [C\,II]}/L_{\rm IR}$ ratio as a function of the FIR luminosity surface density $\Sigma_{\rm IR}$ for MAMBO-9 and various local and high-redshift galaxies. In particular, we show local LIRGs and ULIRGs from GOALS (T. Díaz-Santos et al. 2017), high-z DSFGs from the South Pole Telescope (SPT; J. S. Spilker et al. 2016), $z \gtrsim 6$ quasars (R. Decarli et al. 2018), and several individual galaxies at $z > 5$, including SPT0346-52 at $z = 5.66$ (K. C. Litke et al. 2019, 2022), G09-83808 at $z = 6.03$ (J. A. Zavala et al. 2018b), and B14-65666 at $z = 7.2$ (T. Hashimoto et al. 2019). The IR luminosity is computed from the 1.1 mm continuum using the best-fit FIR SED derived in Section 3.5.1 and integrating over rest-frame 8–1000 μm. We also show in the upper panels maps of the $L_{\rm [C\,II]}/L_{\rm IR}$ ratio for each galaxy, and in the inset panel the distribution of these individual pixels in the $L_{\rm [C\,II]}/L_{\rm IR}$–$\Sigma_{\rm IR}$ plane. MAMBO-9-A and B are consistent with the trend of weaker [C II] in more compact FIR-emitting regions, in both an integrated and spatially resolved sense. Both galaxies show strong [C II] deficits in their central IR-emitting cores, indicating that the [C II] deficit arises from small scales ≲400 pc, similar to what has been found in other high-z DSFGs (K. C. Litke et al. 2019).

Finally, we measure the dust continuum sizes by fitting a 2D Sérsic profile (J. L. Sérsic 1963) to the ALMA continuum imaging. We use the 2D image-fitting code IMFIT[20]

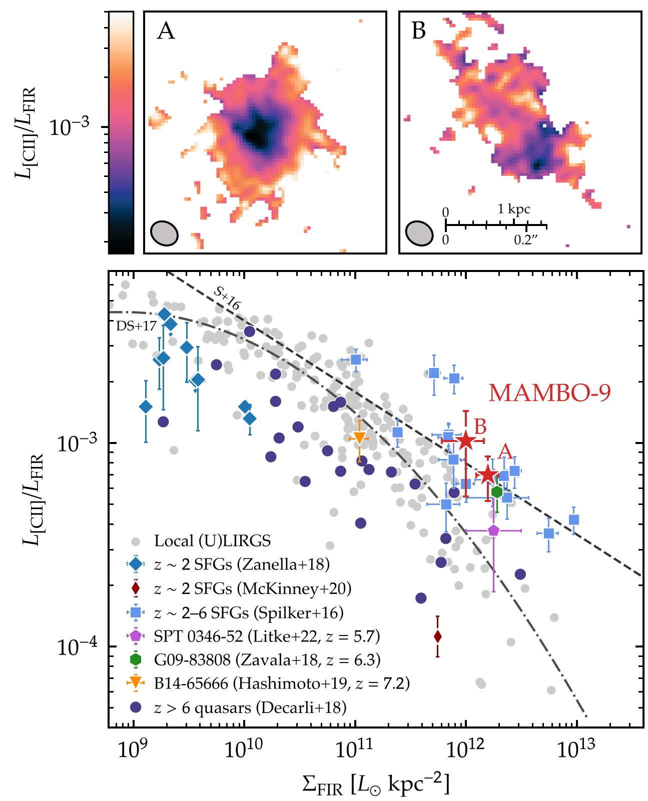

Figure 2. The $L_{\rm [C\,II]}/L_{\rm FIR}$ ratio as a function of $\Sigma_{\rm FIR}$ for the MAMBO-9 system and various local and high-redshift galaxies from the literature. We show local LIRGS and ULIRGS from GOALS (T. Díaz-Santos et al. 2017), $z \sim 2$–6 DSFGs from SPT (J. S. Spilker et al. 2016), $z \gtrsim 6$ quasars (R. Decarli et al. 2018), and several individual $z \gtrsim 5$ galaxies (J. A. Zavala et al. 2018b; T. Hashimoto et al. 2019; K. C. Litke et al. 2019). MAMBO-9 follows the trend of a decreasing $L_{\rm [C\,II]}/L_{\rm FIR}$ ratio as a function of $\Sigma_{\rm FIR}$ (i.e., the "[C II] deficit"). We also show the spatially resolved $L_{\rm [C\,II]}/L_{\rm FIR}$ ratio maps for MAMBO-9-A and B, which follow a similar relationship, indicating that the [C II] deficit arises from small scales ≲400 pc.

[20] https://www.mpe.mpg.de/~erwin/code/imfit/

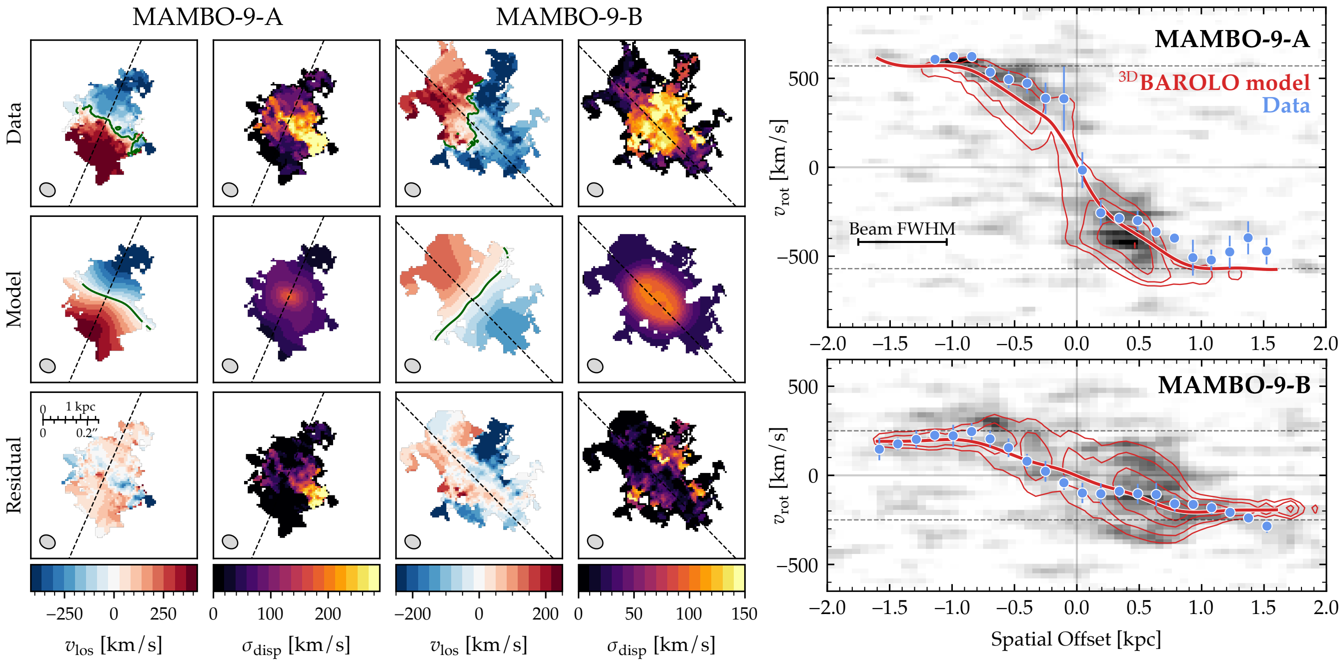

Figure 3. Kinematic modeling of the MAMBO-9 system. Left: velocity (moment 1) and velocity dispersion (moment 2) maps for MAMBO-9-A and B. We show the data, model, and residual for each moment and object. The dashed lines indicate the kinematic major axis (i.e., the mean position angle) adopted in the ^{3D}BAROLO fits. The green contours show $v = 0$ in the moment 1 maps. We adopt $z_A = 5.850$ and $z_B = 5.852$. MAMBO-9-A shows clear rotation across its kinematic major axis. Both components show consistently high velocity dispersions ($\sigma \gtrsim 150$ km s^{-1}), even several kiloparsecs from the galaxy center. Right: major-axis PV diagrams for MAMBO-9-A (top) and B (bottom). The background image shows the PV diagrams extracted from cutouts around the two objects, while the red contours show the PV diagram for the best-fit ^{3D}BAROLO model. The rotation curve extracted along the kinematic major axis is shown in blue, and the corresponding model curve is shown in red.

(P. Erwin 2015)—in particular, the Python wrapper PYIMFIT. We convolve the Sérsic model with the PSF, in this case the Gaussian clean beam returned by the CASA tclean process. To provide realistic uncertainties on the model parameters, we utilize Markov Chain Monte Carlo sampling via the EMCEE Python package. The 2D Sérsic fits to the ALMA dust continuum images yield Sérsic indices of $n = 1.71 \pm 0.03$ and 2.9 ± 0.2 for MAMBO-9-A and B, respectively. This suggests that while MAMBO-9-A is broadly consistent with a normal disk galaxy, MAMBO-9-B has a profile more consistent with a spheroidal galaxy. MAMBO-9-B is also significantly more extended, with an effective radius of $R_{\rm eff} = 1.17 \pm 0.08$ kpc versus 469 ± 4 pc for MAMBO-9-A. The Sérsic fits yield axis ratios of $b/a = 0.75 \pm 0.01$ and 0.80 ± 0.02, which in turn imply disk inclinations of $i = 43.^\circ2 \pm 0.^\circ5$ and $38.^\circ7 \pm 2.^\circ2$ for A and B, respectively (assuming an intrinsic edge-on axis ratio of 0.25; S. Wuyts et al. 2016). These statistical uncertainties do not include systematic uncertainties on the relationship between the morphological axis ratio and disk inclination; for our dynamical mass measurement, we incorporate systematic effects by combining the morphological and kinematic inclinations (see Section 3.2). We note also that while the Sérsic model for MAMBO-9-B was fit to the entire cutout, it converges to capture only the bright core in the southwest corner, and not the extended tail to the northeast. The reported $R_{\rm eff}$ and Sérsic index therefore primarily reflect the core; given the clear tidal disturbance of MAMBO-9-B, however, we caution against overinterpreting these morphological parameters.

3.2. ISM Kinematics

The high resolution of the ALMA [C II] observations facilitates detailed kinematic analysis of both galaxies. We use the ^{3D}BAROLO software (E. M. Di Teodoro & F. Fraternali 2015) to directly fit the data cube to a kinematic model. ^{3D}BAROLO models the observed galaxy as a set of concentric independently rotating rings, approximating a disk. The primary advantage of forward-modeling software like ^{3D}BAROLO, in comparison to direct analysis of position–velocity (PV) diagrams, is the accounting for observational effects such as beam-smearing.

The top row of Figure 3 shows the observed moment 1 and 2 maps (line-of-sight integrated velocity and velocity dispersion) for MAMBO-9-A and B. These moment maps are extracted from the data cube using the SEARCH algorithm in ^{3D}BAROLO, iterating to a noise level of 2σ. Both galaxies show clear velocity gradients across their major axes (indicated by the dashed black lines). At the same time, both galaxies show evidence of disturbed kinematics, with significant asymmetries in the moment 1 map (particularly for MAMBO-9-B) and high velocity dispersions ($\sigma \sim 150$–200 km s^{-1}). We note that the systemic velocity for MAMBO-9-B is offset slightly from MAMBO-9-A, by $\sim$100 km s^{-1}, corresponding to a slightly different redshift of $z = 5.852$.

To analyze the PV diagrams and rotation curves, we apply ^{3D}BAROLO tilted-ring modeling to $1.''35$ square cutouts of each galaxy. We adopt 10 rings in the models, with a separation of $0.''025$, which corresponds to approximately half the resolution of the ALMA observations. We assume a thin disk with a scale height of 60 pc. We conduct a two-stage regularization procedure, first allowing ^{3D}BAROLO to fit all kinematic and geometric parameters (except for the central position, which we determine manually, based on the $v = 0$ contour line in the moment 1 maps). This means that the rotation velocity, velocity dispersion, inclination, and position angle of each ring are fit independently. ^{3D}BAROLO then applies parameter regularization and refits the data, constraining the inclination and position angle to follow a Bezier function while allowing $v_{\rm rot}$ and $\sigma_{\rm disp}$ to vary freely. The derived inclinations range from 44° to 48° for MAMBO-9-A and from 43° to 51° for MAMBO-9-B, similar to, but slightly higher than, the inclinations derived from Sérsic fitting. The middle row of Figure 3 shows the moment 1 and 2 maps of the best-fit $^{\rm 3D}$BAROLO model for each galaxy, and the residuals are shown in the bottom row. We note that both objects show significant positive residuals in the velocity dispersion, particularly along the kinematic minor axis. This may be due to outflowing or kinematically disturbed gas, associated with the close-pass merger.

The rightmost panels of Figure 3 show the major-axis PV diagrams for both galaxies. The ALMA data are shown in gray, and the $^{\rm 3D}$BAROLO model PV diagram is shown with red contours. The blue points show the measured rotation curves extracted from the major axis of the moment 1 maps; the red curve shows the corresponding measurements from the model moment 1 map. Rotation velocities are derived from line-of-sight velocities by $v_{\rm rot} = v_{\rm los}/\sin(i)$, where i is the inclination angle. Here, we adopt the approximate mean of the morphological and kinematic inclination angles for each galaxy; in particular, we take $i = 46° \pm 2°$ for MAMBO-9-A and $i = 45° \pm 6°$ for MAMBO-9-B.

We derive dynamical masses for each component as

$$M_{\rm dyn} = \frac{V_{\rm max}^2 R_{\rm max}}{G}, \quad (1)$$

where $R_{\rm max}$ is the radius of the farthest ring and $V_{\rm max}$ is the maximum rotation velocity. We estimate $V_{\rm rot,max} = 570\ {\rm km\,s^{-1}}$ for MAMBO-9-A and $V_{\rm rot,max} = 250\ {\rm km\,s^{-1}}$ for MAMBO-9-B. The uncertainties in the dynamical mass include the error on the rotation velocity returned by $^{\rm 3D}$BAROLO as well as the uncertainty on the inclination. Since the rotation velocity scales with $1/\sin(i)$ and the dynamical mass scales with v^2, an uncertainty on the inclination of σ_i would correspond to an additional uncertainty on the dynamical mass of $\sigma_{M_{\rm dyn}}/M_{\rm dyn} = 2\sigma_i \cot(i)$. For MAMBO-9-A and B, which have fractional uncertainties on i of ∼4% and ∼13%, this contributes additional 7% and 21% uncertainties to $M_{\rm dyn}$, respectively. We derive dynamical masses of $(1.1 \pm 0.1) \times 10^{11}\, M_\odot$ and $(2.0 \pm 0.5) \times 10^{10}\, M_\odot$ for components A and B, respectively. This corresponds to a merger mass ratio of roughly 1:5—i.e., a minor merger.

We note that these dynamical mass estimates should still be treated as uncertain, particularly for MAMBO-9-B, given the merger state of the two objects and the significant turbulent motion present in both. We measure $V_{\rm rot}/\sigma \approx 4$–8 for MAMBO-9-A, consistent with a rotation-dominated disk. For MAMBO-9-B, we measure $V_{\rm rot}/\sigma \approx 0.5$–3 in the central part of the galaxy, but $\gtrsim$10 in the outskirts. It is thus unclear if we are seeing a rotating system in MAMBO-9-B or simply tidal effects from the merger. We note, however, that it is unlikely that our dynamical mass for MAMBO-9-B is *underestimated*—if anything, it is overestimated due to additional motion induced by the merger—supporting the two galaxies being most likely experiencing a minor merger.

3.3. JWST/NIRCam+MIRI Imaging

Here, we present the new JWST imaging of MAMBO-9, summarized in Figure 4, which provides the first deep resolved view into the rest-frame optical/NIR for this system. We first highlight, in the top-left panel, the previous imaging from HST +Spitzer. MAMBO-9 is not detected in moderately deep HST imaging from CANDELS (N. A. Grogin et al. 2011; A. M. Koekemoer et al. 2011), and only marginally detected in Spitzer/IRAC imaging at 3.6 and 4.5 μm, though unresolved. In fact, prior to JWST, identifying the object as two separate components was only possible with ALMA observations of the dust continuum (C. M. Casey et al. 2019). The bottom panels of Figure 4 show 4″ × 4″ cutouts around MAMBO-9 in six JWST bands: F277W, F356W, F410M, F444W, F770W, and F1800W. We note that MAMBO-9 is undetected in F090W, F115W, F150W, and F200W, even in the moderately deep PRIMER data (F200W 5σ depth ∼29.4 AB mag in a 0.″3 diameter aperture; see Table 1), providing upper limits even deeper than the HST nondetections. MAMBO-9 is faintly detected in F277W (rest-frame ∼4000 Å), appears clearly in F356W, F410M, F444W, and F770W, and is very marginally detected in F1800W. The top-right panels in Figure 4 show a JWST/NIRCam long-wavelength (LW) stack, with the ALMA continuum contours overlaid, and a JWST/NIRCam red green blue (RGB) image with the [C II] contours overlaid.

The NIRCam imaging reveals a faint extended bridge of stellar light between the two components, not visible in the ALMA imaging. This bridge is quite red, suggesting it is significantly dust-attenuated or hosts an older stellar population. Moreover, it is largely aligned with the kinematic axis of each component (see Section 3.2), suggesting that it may originate from tidal forces induced by the close passage of the two objects.

The MIRI F770W and F1800W bands probe the rest-frame NIR at $z \sim 6$, which is subject to far less attenuation than the UV/optical. Due to the shallow depth of the F1800W imaging, MAMBO-9 is only marginally detected, and its morphology is unclear. In F770W, however, MAMBO-9 is clearly detected and exhibits three clear peaks—one central peak in MAMBO-9-A and two in MAMBO-9-B. The peak F770W positions are slightly offset from the NIRCam stack; to illustrate this, we indicate the positions of the three SNR peaks in F770W on the NIRCam stack in Figure 4. The F770W peak positions largely align with the ALMA continuum peaks, indicating that the majority of stellar mass arises from the FIR-emitting regions. However, at the position of the NE F770W peak in MAMBO-9-B, both the ALMA dust continuum and NIRCam imaging are quite faint, indicating perhaps the presence of an older stellar population.

3.4. JWST/NIRSpec Spectrum of MAMBO-9-B

As noted in Section 2.2, MAMBO-9-B was recently observed with JWST/NIRSpec as part of the CAPERS survey (GO#6368; PI: M. Dickinson). MAMBO-9-B was observed with the PRISM disperser (covering 0.6–5.3 μm at $R \sim 100$) with an exposure time of 4.74 hr. The spectrum (shown in Figure 5) yields detections of [O II] λλ3727, 3729, Hβ, [O III] λλ4959, 5007, Hα, and [S II] λλ6347, 6371. We measure line fluxes by fitting Gaussian models to the PRISM spectrum, including a variable local continuum and flexible line width. We measure a redshift from the PRISM spectrum of $z = 5.86 \pm 0.01$, consistent with the ALMA [C II] redshift.

We measure the nebular dust attenuation from the Balmer decrement. We measure integrated line fluxes in Hα and Hβ of

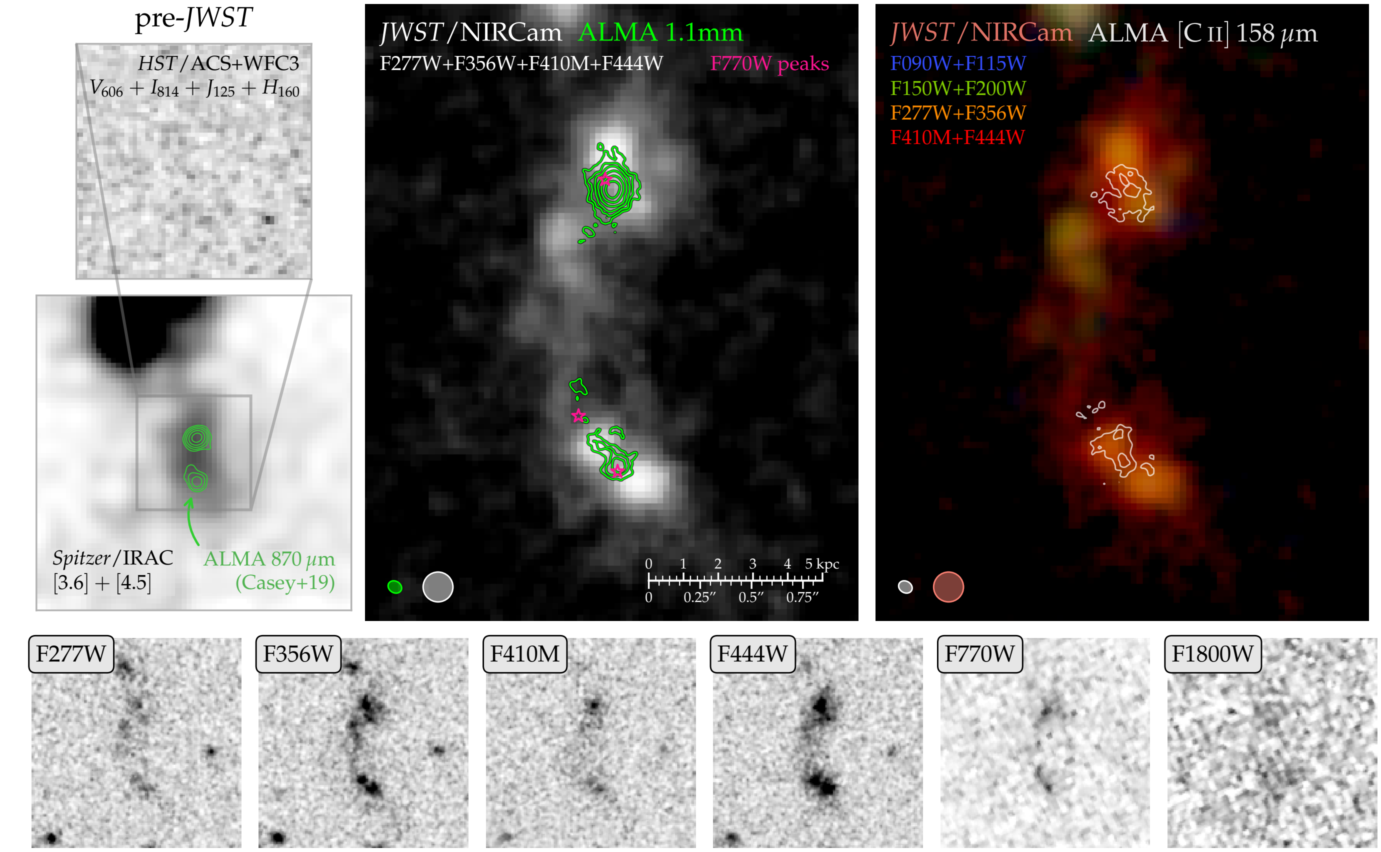

Figure 4. New JWST imaging of MAMBO-9, illustrating the utility of JWST+ALMA for spatially resolving high-z DSFGs. Top left: stacked cutout of Spitzer/IRAC [3.6] + [4.5]. MAMBO-9 was marginally detected in IRAC imaging, though completely unresolved; identifying the two separate components required targeted ALMA continuum imaging (C. M. Casey et al. 2019). The zoomed inset shows a stacked cutout from combining four HST bands (F606W, F814W, F125W, and F160W) from CANDELS (N. A. Grogin et al. 2011; A. M. Koekemoer et al. 2011), in which MAMBO-9 was undetected. Top center: inverse-variance-weighted stack of the JWST/NIRCam LW bands, which have been PSF-matched to F444W. The green contours show the high-resolution ALMA imaging of the 1.1 mm dust continuum as in Figure 1. Top right: false-color RGB image constructed from all eight PSF-matched NIRCam bands. The white contours show the [C II] 158 μm flux. The resolution of the ALMA data is ~3 times better than F444W, shown as the ellipses in the bottom-left corner. The bright dust-continuum-emitting regions are fainter in the rest-frame optical, suggesting that there is significant obscuration in the core of both galaxies. Bottom: JWST/NIRCam+MIRI imaging of MAMBO-9. The panels show 4″ × 4″ cutouts in F277W, F356W, F410M, F444W, F770W, and F1800W. MAMBO-9 is undetected at wavelengths shortward of 2 μm, even in deep JWST imaging.

$4.0^{+0.1}_{-0.1} \times 10^{-18}$ and $4.9^{+0.6}_{-0.6} \times 10^{-19}$ erg s^{-1} cm^{-2}, respectively. The ratio of Hα/Hβ = $8.3^{+1.2}_{-0.9}$ implies a nebular dust attenuation of $A_V = 3.6^{+0.5}_{-0.4}$, assuming a D. Calzetti et al. (2000) attenuation law. We measure a high rest-frame EW, $\mathrm{EW}_0(\mathrm{H}\alpha) = 640^{+44}_{-40}$ Å. The Hα luminosity, corrected for attenuation via the Balmer decrement, implies an SFR of $\mathrm{SFR}(\mathrm{H}\alpha) = 133^{+54}_{-33}\,M_\odot\,\mathrm{yr}^{-1}$, using the calibration from R. C. Kennicutt & N. J. Evans (2012). This remains somewhat below the global SFR inferred from [C II] (~290 $M_\odot$ yr^{-1}) or the FIR (~390 $M_\odot$ yr^{-1}). This difference likely reflects the limited physical extent of MAMBO-9-B sampled by the NIRSpec slit. Even with standard pipeline path-loss corrections applied, the ~0″.2 × 0″.4 size of the MSA shutter is smaller than the full extent of MAMBO-9-B, making any flux measurement a lower limit on the total across the galaxy.

3.5. SED Fitting

With the new JWST and high-resolution ALMA data, we aim to better physically constrain the stellar properties of the MAMBO-9 system. We first fit the FIR SED on its own, to characterize the dust emission and constrain the dust temperature and emissivity (Section 3.5.1); we then perform an integrated energy-balance fit to the full rest-UV-to-FIR SED (Section 3.5.2); and finally we perform a spatially resolved energy-balance fit, which we use to validate the integrated results and examine the underlying stellar morphology of the system (Section 3.5.3).

3.5.1. FIR SED Fitting

We begin by fitting the FIR SED on its own, absent any assumptions about energy balance, in order to characterize the dust emission and to provide the dust temperature and emissivity used in the energy-balance fits below. The existing literature photometry for MAMBO-9, from the rest-frame UV to FIR, is summarized in Table 2 of C. M. Casey et al. (2019); we adopt these mid-IR (MIR) and FIR measurements in our SED fitting. We include the new ALMA Band 7 data ($\lambda \sim 1.1$ mm), with measured fluxes of 2.7 ± 0.1 and 0.9 ± 0.1 mJy for MAMBO-9-A and B, respectively. Note that we omit the unresolved MAMBO, AzTEC, and SCUBA-2 850 μm data, as the higher-resolution ALMA observations sufficiently cover this wavelength range, and at much higher SNR. We include the nondetections from Spitzer/MIPS, Herschel/PACS+SPIRE, and SCUBA-2 450 μm as upper limits.

We fit the FIR SED to a modified blackbody+power law, as described in C. M. Casey (2012) and P. M. Drew &

Table 1
New Photometry from JWST and ALMA

Band	Exp. Time (ks)	Wavelength	5σ Depth	Units	MAMBO-9-A	MAMBO-9-B	Bridge
F090W	5.03	0.9 μm	28.4	nJy	<28	<24	<12
F115W	6.79	1.15 μm	28.6	nJy	<23	<20	<9
F150W	5.54	1.5 μm	28.7	nJy	<20	<17	<8
F200W	12.56	2.0 μm	29.4	nJy	18 $\pm$ 3	<9	6 $\pm$ 1
F277W	5.54	2.77 μm	29.4	nJy	73 $\pm$ 4	39 $\pm$ 3	11 $\pm$ 2
F356W	5.43	3.56 μm	29.5	nJy	131 $\pm$ 3	85 $\pm$ 3	13 $\pm$ 1
F410M	5.03	4.10 μm	28.6	nJy	159 $\pm$ 8	109 $\pm$ 7	18 $\pm$ 3
F444W	4.70	4.44 μm	29.0	nJy	227 $\pm$ 5	188 $\pm$ 5	19 $\pm$ 2
F770W	1.78	7.7 μm	26.2	nJy	497 $\pm$ 81	270 $\pm$ 59	<64
F1800W	1.78	18 μm	24.4	nJy	886 $\pm$ 267	1050 $\pm$ 237	<293
ALMA-B7	4.35	1.1 mm	⋯	mJy	2.7 $\pm$ 0.1	0.9 $\pm$ 0.1	<0.1

Note. Depths are 5σ point-source-equivalent limits at the position of MAMBO-9, measured in 0$''$.3 diameter (NIRCam) and 0$''$.5 diameter (MIRI) circular apertures on the native-resolution mosaics. Nondetections are reported as 3σ limits. The "bridge" region is indicated in the inset panel of Figure 6.

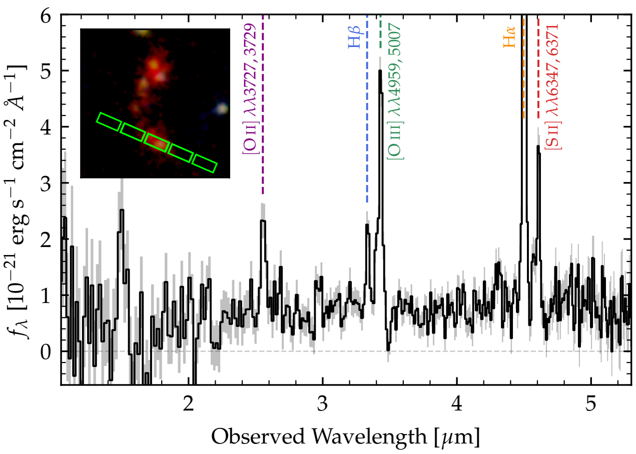

Figure 5. JWST/NIRSpec PRISM spectrum of MAMBO-9-B from CAPERS (GO#6368). The inset panel shows the NIRCam composite RGB image of MAMBO-9 with the NIRSpec slitlet overlaid. We mark the positions of the detected emission lines.

C. M. Casey (2022); that is, the FIR SED follows a modified blackbody in the Rayleigh–Jeans tail and switches to a power law in the Wien tail in order to account for the presence of multiple increasingly hot, increasingly faint dust components. In the absence of strong constraints at rest-frame 10–100 μm, we fix the power-law slope $\alpha_{\rm MIR} = 4.0$. We adopt an optically thin blackbody for MAMBO-9-B, while for MAMBO-9-A we adopt the more general opacity model described in C. M. Casey et al. (2019), in which $\tau = 1$ at $\lambda = 200\,\mu$m. We perform fitting using a Markov Chain Monte Carlo routine with flat priors on $L_{\rm IR}$, $T_{\rm dust}$, and β, and correct for the effects of heating by and decreasing contrast against the cosmic microwave background, following E. da Cunha et al. (2013).

The resulting FIR-only fits are shown in orange in Figure 6. For MAMBO-9-A, we derive a dust temperature of $59.0^{+6.3}_{-6.6}$ K and an IR luminosity of $(4.2^{+1.0}_{-0.9}) \times 10^{12}\,L_\odot$. For MAMBO-9-B, we derive a dust temperature of $37.9^{+5.7}_{-5.8}$ K and an IR luminosity of $(2.6^{+1.2}_{-1.0}) \times 10^{12}\,L_\odot$. Using the calibration from R. C. Kennicutt & N. J. Evans (2012), these IR luminosities correspond to obscured SFRs of $\mathrm{SFR_{IR}} = 620^{+150}_{-130}$ and $390^{+180}_{-150}\,M_\odot\,\mathrm{yr}^{-1}$ for MAMBO-9-A and B, respectively. These are slightly different from, but consistent with, the measurements from C. M. Casey et al. (2019).

3.5.2. Integrated Energy-balance SED Fit

We next fit the entire SED from the rest-frame UV to FIR under an energy-balance assumption using BAGPIPES (A. C. Carnall et al. 2018). BAGPIPES uses the nested sampling algorithm MULTINEST to conduct Bayesian inference of galaxy physical properties based on user-defined sets of model components. We adopt the BPASS library stellar population models (J. J. Eldridge et al. 2017) and a nonparametric SFH model defined by the $\Delta\log(\mathrm{SFR})$ in adjacent time bins (see J. Leja et al. 2019). We construct six fixed-age bins at 0–10, 10–30, 30–100, 100–200, 200–500, and 500–800 Myr. We use a "bursty continuity" prior (S. Tacchella et al. 2022)—e.g., a t distribution with $\sigma = 1.0$ and $\nu = 2$. This prior allows for sharp discontinuities between time bins, in particular, allowing for a recent starburst. We allow the metallicity to vary from 0 to $2.5\,Z_\odot$ with a uniform prior. Nebular emission is included, with $\log U$ allowed to vary from -4 to -1. We adopt an S. Salim et al. (2018) parameterization dust attenuation curve, with A_V allowed to vary from 0 to 8 and the power-law deviation from a D. Calzetti et al. (2000) law δ from -0.5 to 0.5. We include additional dust attenuation around "birthclouds" (i.e., stars younger than 10 Myr) via a multiplicative factor η, which is allowed to vary from 1 to 10 with a uniform prior. We found this was necessary to reproduce the extreme SFRs implied by the FIR without significant flux boosting from strong emission lines in the NIRCam bands. We note that allowing for more dust attenuation around birthclouds means that the mass-weighted A_V can be higher than 8, the nominal maximum of the prior. We assume energy balance, such that the total energy absorbed by dust is reradiated in the FIR/submillimeter. For the dust emission, we have modified BAGPIPES to include the same modified blackbody+power-law form used for the FIR-only fits (Section 3.5.1). We fix $T_{\rm dust}$ and β to their best-fit FIR-only values; we find this provides a substantially better description of the FIR SED than the BAGPIPES default B. T. Draine & A. Li (2007) templates, particularly for MAMBO-9-B. Photometric uncertainties are calibrated via the random-aperture method described in Section 2.2 (see Table 1).

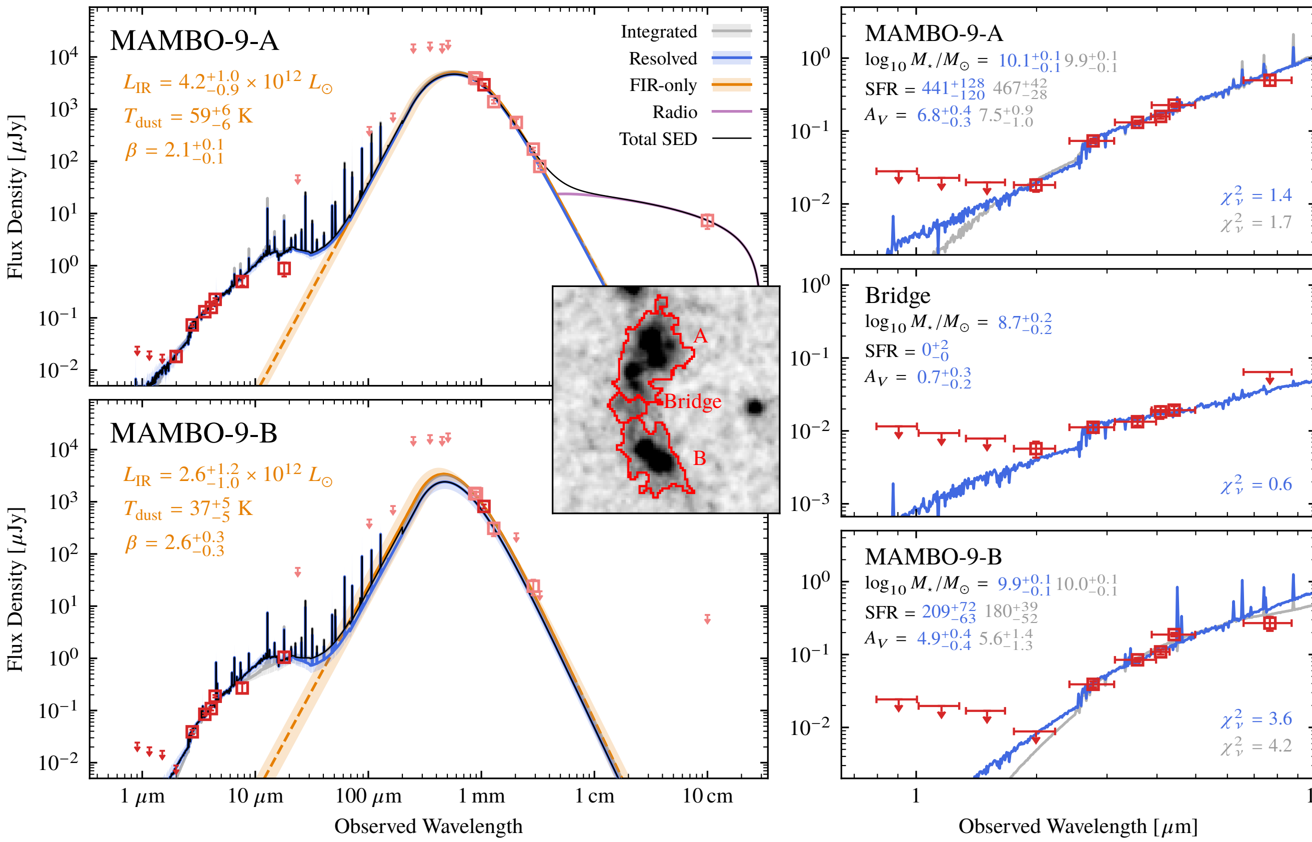

Figure 6. SEDs and best-fit models for MAMBO-9. The FIR-only SED fits are shown in orange, the integrated energy-balance fits in gray, and the spatially resolved energy-balance fits in blue. Existing photometry as compiled by C. M. Casey et al. (2019) is shown in light red, while the new JWST and ALMA photometry from this work is shown in dark red. The right panels show zoom-ins of the optical–NIR SEDs for MAMBO-9-A and B, and the bridge between the two, as extracted from the regions shown in the inset cutout; the reduced χ^2 values of the integrated and resolved fits are quoted in each panel.

Figure 6 shows the full panchromatic SED for MAMBO-9-A and B; the best-fit BAGPIPES fits to the integrated photometry are shown in gray. The right panels show zoom-ins to the optical/NIR portion of the SED. The best-fit SED for MAMBO-9-A includes a moderate Balmer break, indicating an older stellar population, required by the NIRCam/F200W photometry. The SED fit yields a stellar mass of $\log M_\star/M_\odot = 9.9^{+0.1}_{-0.1}$, an SFR of SFR $= 467^{+42}_{-28}\ M_\odot\ \mathrm{yr}^{-1}$, and a dust attenuation of $A_V = 7.5^{+0.9}_{-1.0}$. For MAMBO-9-B, the SED fit yields a stellar mass of $\log M_\star/M_\odot = 10.0^{+0.1}_{-0.1}$, an SFR of SFR $= 180^{+39}_{-52}\ M_\odot\ \mathrm{yr}^{-1}$, and a dust attenuation of $A_V = 5.6^{+1.4}_{-1.3}$. These SFRs are somewhat lower than those derived from our dedicated FIR-only fits (620 and 390 $M_\odot\ \mathrm{yr}^{-1}$), reflecting the different timescales probed by the FIR calibration versus SED fitting. We adopt these integrated stellar masses as our fiducial mass measurements (Table 2).

3.5.3. Spatially Resolved SED Fitting

Given the complex multiwavelength morphology presented in Section 3.3, with optical/NIR emission somewhat decoupled from the FIR emission, we additionally perform spatially resolved SED fitting to capture variations in the dust attenuation and stellar population properties across the two galaxies and validate our integrated SED fitting results. While the SNR is not sufficient to perform pixel-by-pixel SED fitting, we construct 2D spatial bins using the `vorbin` package in Python. `vorbin` takes a 2D image and noise map as input and constructs spatial Voronoi bins to yield a specified target SNR per bin. We define the bins based on a composite of the NIRCam LW stack (shown in Figure 4) and the ALMA dust continuum map, which has been *uv*-tapered by 0.″13 and resampled to match the JWST/F444W resolution. We set the target SNR to 30, which we find produces a reasonable number of bins (90) with sufficient SNR in each band to derive physical properties. We note that we combined multiple Voronoi bins to construct the extraction apertures for MAMBO-9-A and B used in the integrated SED fits in the previous section (shown in the inset panel of Figure 6). We refer to the remaining apertures as probing the "bridge" between the two objects.

For each bin, we fit the SED to the JWST/NIRCam+MIRI photometry and the *uv*-tapered ALMA 1.1 mm dust continuum map, using the same stellar, nebular, and dust attenuation priors as our integrated `bagpipes` run, and the same modified blackbody+power-law dust emission model with T_{dust} and β fixed to their FIR-only values. We require energy balance within each bin. Because the spatially resolved fitting depends on the relative spatial distribution of the dust and the stellar light, the choice of PSF homogenization is not straightforward. We elect to homogenize the NIRCam bands to the F444W PSF (and adopt the corresponding *uv*-tapered ALMA map), but include MIRI/F770W at its native resolution (FWHM ∼0.″25 versus F444W ∼0.″15). We exclude F1800W from the resolved fit, due to its substantially larger PSF (FWHM ∼0.″6). This has the potential to dilute the MIRI flux between bins. We note that we explored homogenizing all

Table 2
Measured and Derived Properties for MAMBO-9

Property	Units	MAMBO-9-A	MAMBO-9-B
z	…	5.8500	5.8518
R.A.	hms	10:00:26.358	10:00:26.357
Decl.	dms	+02:15:27.92	+02:15:26.59
From ALMA FIR continuum measurements…			
$T_{\rm dust}$	K	59^{+6}_{-6}	37^{+5}_{-5}
β	…	$2.1^{+0.1}_{-0.1}$	$2.6^{+0.3}_{-0.3}$
$L_{\rm IR}$	$10^{12}\,L_\odot$	$4.2^{+1.0}_{-0.9}$	$2.6^{+1.2}_{-1.0}$
$\Sigma_{\rm IR}$	$10^{11}\,L_\odot$ kpc^{-2}	$15.8^{+3.9}_{-3.4}$	$10.0^{+4.6}_{-3.9}$
SFR$_{\rm IR}$	$M_\odot$ yr^{-1}	620^{+150}_{-130}	390^{+180}_{-150}
$M_{\rm dust}$[a]	$10^8\,M_\odot$	13 ± 3	$1.9^{+1.3}_{-0.8}$
Sérsic n	…	1.71 ± 0.03	2.9 ± 0.2
$R_{\rm eff}$	pc	469 ± 4	1170 ± 80
b/a	…	0.75 ± 0.01	0.80 ± 0.02
i	deg	43.2 ± 0.5	38.7 ± 2.2
From ALMA [C II] *158 μ m line measurements…*			
$L_{\rm [C\,II]}$	$10^9\,L_\odot$	3.1 ± 0.2	3.3 ± 0.3
SFR$_{\rm [C\,II]}$	$M_\odot$ yr^{-1}	270 ± 190	290 ± 200
$M_{\rm dyn}$	$10^{10}\,M_\odot$	10.6 ± 0.9	2.0 ± 0.5
From broadband SED fitting…			
$M_\star$	$10^9\,M_\odot$	$8.9^{+1.2}_{-0.8}$	$9.6^{+3.6}_{-2.2}$
A_V	mag	$7.5^{+0.9}_{-1.0}$	$5.6^{+1.4}_{-1.3}$
SFR	$M_\odot$ yr^{-1}	467^{+42}_{-28}	180^{+39}_{-52}
From mass budget analysis…			
$M_{\rm gas}$	$10^{10}\,M_\odot$	$9.5^{+0.9}_{-0.9}$	$1.0^{+0.5}_{-0.6}$
$f_{\rm gas}$	…	90^{+1}_{-1}%	50^{+15}_{-23}%

Note.
[a] Dust masses are taken from C. M. Casey et al. (2019), derived from 3 mm continuum observations.

bands to F770W, or omitting F770W entirely, but found this led to substantially worse fits than the integrated SED fitting: in the former, the fits were unable to match the observed ALMA 1.1 mm continuum flux, while in the latter, they significantly overpredicted the per-component MIRI fluxes. With our adopted scheme, by contrast, the resolved model reproduces both well. All photometric uncertainties are measured with the random-aperture method of Section 2.2.

Figure 7 shows the results of our spatially resolved SED fitting procedure. In particular, we show the stellar mass surface density $\Sigma_\star$, SFR surface density $\Sigma_{\rm SFR}$, dust attenuation A_V, and inferred Hα EW in each 2D bin. For MAMBO-9-A, the bulk of the stellar mass and recent star formation is concentrated in the central core, which is highly obscured ($A_V > 10$). MAMBO-9-B is also significantly obscured, with a mass-weighted $A_V \sim 5$, but exhibits elevated Hα EWs (EW$_0$ reaching ∼1000 Å) in its less-obscured outskirts. This SED-inferred EW is consistent with the NIRSpec spectrum of MAMBO-9-B (Section 3.4), which yields EW$_0$(Hα) = 640^{+44}_{-40} Å and a nebular $A_V = 3.6^{+0.5}_{-0.4}$ from the Balmer decrement. In the future, deep integral field unit spectroscopy could be used to more robustly examine the spatial variation in the dust attenuation, as well as other properties, such as gas-phase metallicity.

The final SEDs for MAMBO-9-A and B, constructed by summing the SEDs for each spatial bin, are shown in blue in Figure 6. For MAMBO-9-A, we recover a stellar mass of $\log M_\star/M_\odot = 10.1^{+0.1}_{-0.1}$, an SFR of SFR = $441^{+128}_{-120}\,M_\odot$ yr^{-1}, a mass-weighted dust attenuation of $A_V = 6.8^{+0.4}_{-0.3}$, and an F444W light-weighted attenuation of $A_V \approx 4.5$. For MAMBO-9-B, we recover $\log M_\star/M_\odot = 9.9^{+0.1}_{-0.1}$, SFR = $209^{+72}_{-63}\,M_\odot$ yr^{-1}, a mass-weighted $A_V = 4.9^{+0.4}_{-0.4}$, and a light-weighted $A_V \approx 4.0$. For the bridge, we recover $\log M_\star/M_\odot = 8.7^{+0.2}_{-0.2}$, with negligible recent star formation and low attenuation ($A_V = 0.7^{+0.3}_{-0.2}$). The resolved stellar masses agree with the integrated values to within ∼0.15 dex, and the resolved SEDs provide statistically comparable—indeed, in each case, marginally better—fits than the integrated SEDs: the reduced χ^2 values are 1.4 (resolved) versus 1.7 (integrated) for MAMBO-9-A, and 3.6 versus 4.2 for MAMBO-9-B.

The resolved fits highlight that the mass-weighted attenuation for MAMBO-9-A ($A_V \approx 6.8$) substantially exceeds the light-weighted value (≈4.5). The rest-optical light is dominated by the least-obscured sightlines, so a purely luminosity-weighted measurement systematically underestimates the obscuration of the optically faint regions that nonetheless hold much of the stellar mass and dominate the dust emission. This is an important caveat for interpreting A_V derived from integrated photometry of high-z DSFGs with complex dust–star geometries: in the absence of a multicomponent dust model, unresolved modeling effectively constrains the light-weighted attenuation and may substantially understate the true obscuration.

4. Discussion

4.1. A Highly Dust-obscured Merger at z = 5.85

MAMBO-9 is among the highest-redshift spectroscopically confirmed DSFGs, and provides valuable insight into the extreme star formation conditions of massive galaxies in the first Gyr. From our spatially resolved SED fitting, we derive a high stellar mass density in the central region of MAMBO-9-A, $\log \Sigma_\star/(M_\odot\,{\rm kpc}^{-2}) \gtrsim 9$, similar to DSFGs and massive quiescent galaxies at cosmic noon (e.g., K. A. Suess et al. 2021). Moreover, we find that the bulk of the recent star formation, traced by the dust and [C II] emission, originates from the compact central core of each object, from clouds with very high dust attenuation $A_V \gtrsim 10$. This is similar to what is seen in the nuclear region of Arp 220, a local ULIRG comprised of two merging starbursts, each with highly concentrated nuclear disks (N. Scoville et al. 2017). Estimates of the nuclear attenuation in Arp 220 range from $A_V \sim 6$ to ∼100 (M. Haas et al. 2001; H. Engel et al. 2011), with recent measurements from JWST/NIRSpec ∼11–14 (M. Perna et al. 2024). Recent spatially resolved studies using JWST have found potentially substantial optically thick substructures in relatively normal massive galaxies at $z \sim 3$, suggesting that this could be a common feature in massive galaxies (Y. Cheng et al. 2025). Future JWST spectroscopy could confirm the high dust attenuation in MAMBO-9, via direct measurements of the Balmer and/or Paschen line decrements.

The JWST imaging has revealed a continuous bridge of material connecting MAMBO-9-A and B, likely a tidal tail from a recent close pass between the two objects. This would be among the highest-redshift tidal tails detected (although see also Y. Sugahara et al. 2025). Interestingly, the tidal tail is itself quite red, and moderately dust-obscured ($A_V \sim 1$), indicating significant dust enrichment even ∼4 kpc from the central star-forming core(s). Moreover, the tidal tail/bridge between the two objects comprises $\sim 5 \times 10^8\,M_\odot$ ∼3% of the total stellar mass of the MAMBO-9 system.

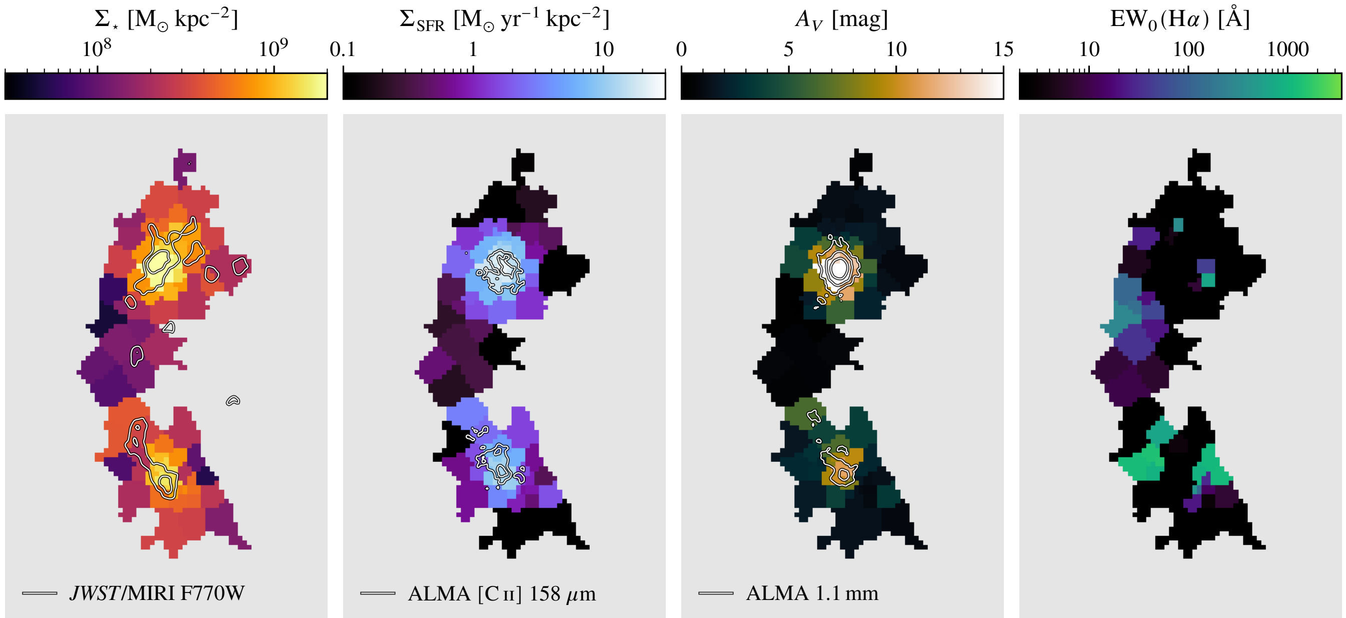

Figure 7. Results from our spatially resolved SED fitting procedure. From left to right, we show maps of the best-fit stellar mass surface density $\Sigma_\star$, SFR surface density $\Sigma_{\rm SFR}$ (over the last 100 Myr), dust attenuation A_V (including additional attenuation toward young stars), and EW EW$_0$(Hα) in each Voronoi bin.

We note that the new MIRI F1800W data do not provide any evidence for a buried AGN in MAMBO-9, which would provide a strong MIR flux enhancement (e.g., R. J. Ivison et al. 2004). Though both components are only marginally detected, the measurements are 2 orders of magnitude below Spitzer/MIPS 24 μm limits. The SEDs of MAMBO-9-A and B are consistent with stellar emission dominating at rest-frame $\sim$2–3 μm, with no need for a significant AGN torus component.

4.2. Mass Budget

The [C II] kinematics and broadband SED fitting presented in this work provide independent constraints on the dynamical and stellar masses, respectively, of the MAMBO-9 system. Here, we incorporate existing constraints on the gas and dust mass to discuss the mass budget of MAMBO-9, with particular focus on the conversion factors to derive gas masses.

First, we consider the $L_{\rm CO}$ to $M_{\rm H_2}$ conversion factor, $\alpha_{\rm CO}$. While the Milky Way ratio of $\alpha_{\rm CO} \sim 4.5\,M_\odot$ (K km s^{-1} pc^{-2})$^{-1}$ (6.5 including He gas) is commonly adopted, the conversion factor is known to scale with metallicity. Here, we assume the helium-corrected $\alpha_{\rm CO}$ scaling from G. Accurso et al. (2017, their Equation (25)), ignoring the dependence on SFR, which is marginal compared to the dependence on metallicity. We adopt $L'_{\rm CO}(6-5) = (1.4 \pm 0.9) \times 10^{10}$ K km s^{-1} pc^{-2} for MAMBO-9-A and $(2.3 \pm 0.7) \times 10^9$ K km s^{-1} pc^{-2} for MAMBO-9-B (C. M. Casey et al. 2019). We assume that the CO spectral line energy distribution (SLED) follows the average for high-z DSFGs, such that $I_{\rm CO(6-5)}/I_{\rm CO(1-0)} = 10^{+30}_{-5}$ (C. M. Casey et al. 2014), i.e., $L'_{\rm CO(1-0)} \sim 3.6 L'_{\rm CO(6-5)}$. We then calculate the H$_2$ mass as $\alpha_{\rm CO} L'_{\rm CO(1-0)}$.

Second, provided there are observations on the Rayleigh–Jeans tail, gas masses can also be estimated from dust masses assuming a gas-to-dust ratio (GDR; e.g., N. Scoville et al. 2016), which is known to also scale with metallicity. We adopt the dust masses measured in C. M. Casey et al. (2019): $(1.3 \pm 0.3) \times 10^9\,M_\odot$ and $(1.9^{+1.3}_{-0.8}) \times 10^8\,M_\odot$ for components A and B, respectively, which are measured from 3 mm continuum imaging. We assume the GDR scaling with metallicity from A. Rémy-Ruyer et al. (2014).

Figure 8 shows the mass budget of MAMBO-9-A and B as a function of the metallicity assumed in computing $\alpha_{\rm CO}$ and the GDR, which are shown in the two additional axes at the top. The dynamical mass is shown as a black horizontal line, and the total baryonic mass ($M_\star + M_{\rm dust} + M_{\rm gas}$) is shown in blue and red for gas mass calculations based on $\alpha_{\rm CO}$ and GDR, respectively. We mark with stars the points at which the total baryonic mass matches the dynamical mass.

The dynamical mass measurements require gas masses of $9.5^{+0.9}_{-0.9} \times 10^{10}\,M_\odot$ for MAMBO-9-A and $1.0^{+0.5}_{-0.6} \times 10^{10}\,M_\odot$ for MAMBO-9-B (see Table 2). This corresponds $\alpha_{\rm CO} \sim 1$–2, consistent with other DSFGs (D. Downes & P. M. Solomon 1998; L. J. Tacconi et al. 2008; R. Genzel et al. 2010; M. S. Bothwell et al. 2013; J. A. Zavala et al. 2022) and in stark contrast to expectations for low-metallicity environments, where $\alpha_{\rm CO}$ can reach $\sim$100 (S. C. Madden et al. 2020; L. A. Boogaard et al. 2021; Q. Jiao et al. 2021; R. L. Sanders et al. 2023). Similarly, our results require a GDR of $\sim$55–75. These results are consistent with slightly supersolar metallicity, implying an evolved stellar population/ISM already by $z = 5.85$.

Our new JWST-derived stellar masses also reaffirm the high dust-to-stellar mass ratio in MAMBO-9. Combined with the dust masses from C. M. Casey et al. (2019), we find $M_{\rm dust}/M_\star = 0.14 \pm 0.03$ for MAMBO-9-A and $0.02^{+0.01}_{-0.01}$ for MAMBO-9-B ($\log M_{\rm dust}/M_\star \approx -0.84$ and -1.7), placing MAMBO-9-A at the extreme high end of the values measured for DSFGs out to $z \sim 5$ (D. Donevski et al. 2020) and comparable to the most extreme $z \gtrsim 6$ systems with joint JWST +ALMA constraints (H. S. B. Algera et al. 2026). Such ratios are difficult to reconcile with stellar nucleosynthesis: the integrated metal yield of a P. Kroupa (2002) IMF is only $\sim$5% (F. Vincenzo et al. 2016), and this only reaches $\sim$6%–7% for a top-heavy IMF with every metal atom locked into grains (J. Witstok et al. 2023). While MAMBO-9-B ($\sim$2%) remains

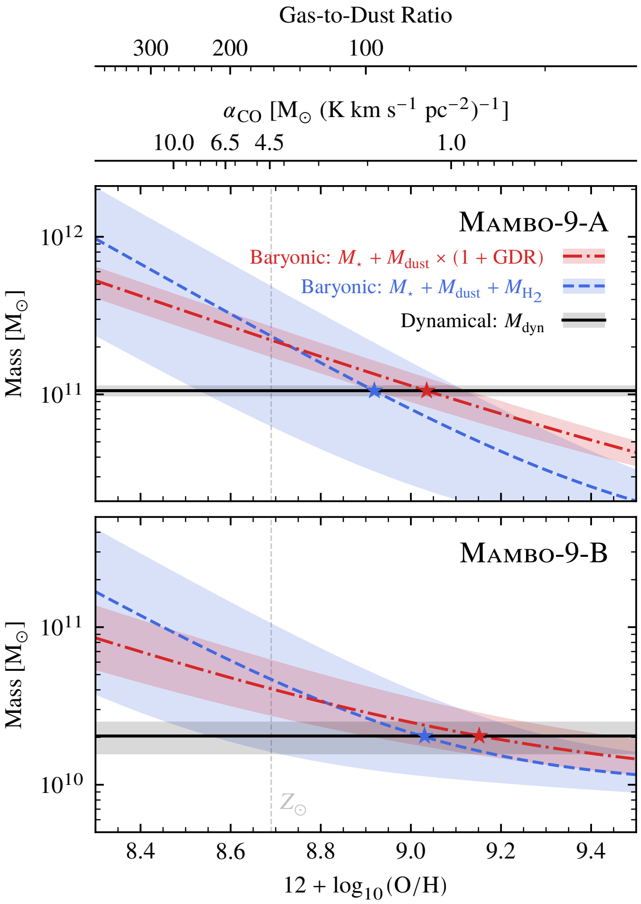

Figure 8. Mass budget of MAMBO-9-A and B as a function of the metallicity used to compute the gas mass. The red/blue lines and shaded regions indicate the total baryonic mass ($M_\star + M_{dust} + M_{gas}$), computed assuming either α_{CO} (blue dashed line) or a GDR (red dotted–dashed line), adopting standard calibrations with metallicity for both (see the text). Note that the CO-based gas mass includes the uncertainty on the CO SLED. The black line and shaded region indicate the dynamical mass constraint derived in this work. The new constraints on the stellar and dynamical masses require $\alpha_{CO} \sim$ 1–2 or GDR $\sim$ 55–75, consistent with supersolar metallicity.

within this budget, MAMBO-9-A exceeds the absolute maximum by a factor of $\sim$2; indeed, MAMBO-9 (as MORA-4) was among the sources flagged by J. Witstok et al. (2023) as formally exceeding the theoretical maximum dust-to-stellar mass ratio. This may reflect additional dust formation processes at play beyond standard asymptotic giant branch star or supernova production channels—for instance, by efficient grain growth in the ISM (M. J. Michałowski 2015; A. Leśniewska & M. J. Michałowski 2019). It is unlikely, however, that the high dust-to-stellar mass ratio stems from an order-of-magnitude underestimate of the stellar mass, as the gas mass inferred from CO already accounts for $\sim$90% of M_{dyn} in MAMBO-9-A—there is little room to hide much more mass in stars.

4.3. The Environment around MAMBO-9

Finally, we discuss whether MAMBO-9 resides in an overdense environment. For many years, it has been suggested that unusually massive and rare galaxies—including quasars (B. P. Venemans et al. 2002, 2005, 2007; K. Shimasaku et al. 2003; E. Kuiper et al. 2011) and DSFGs (S. C. Chapman et al. 2008; H. Dannerbauer et al. 2014; C. M. Casey 2016; C.-L. Hung et al. 2016; D. P. Marrone et al. 2018; T. B. Miller et al. 2018; I. Oteo et al. 2018)—can serve as beacons of the most massive structures still in the protocluster phase before virialization. Indeed, cosmological simulations predict massive DSFGs to sit in the progenitor structures of eventual galaxy clusters (T. B. Miller et al. 2015; Y.-K. Chiang et al. 2017). Recent JWST results from the JADES (D. J. Eisenstein et al. 2026) and FRESCO (P. A. Oesch et al. 2023) surveys reveal a large-scale overdensity at $z \sim 5.2$ in GOODS-N (F. Sun et al. 2024; T. Herard-Demanche et al. 2025), around the SMGs HDF850.1 ($z = 5.184$) and GN10 ($z = 5.303$). Where previous spectroscopic efforts had identified one quasar and $\sim$11 galaxies at similar redshifts (F. Walter et al. 2012), these recent NIRCam WFSS grism observations have detected $\sim$100 Hα emitters at the same redshift within a (15 cMpc)^3 region.

The story of MAMBO-9 appears to follow a similar pattern: several Lyα emitters have been serendipitously identified at $z \approx$ 5.84–5.88 nearby, largely from Keck or Very Large Telescope (VLT) spectroscopy (G. Hasinger et al. 2018; L. Pentericci et al. 2018; K. B. Schmidt et al. 2021; B. Epinat et al. 2024), and another unique optically dark DSFG, COS-3mm-1 (C. C. Williams et al. 2019) has a tentative CO(6–5) line detection at $z = 5.85$ (J. A. Zavala 2021), though it is $\sim$0°.5 ($\sim$70 cMpc) away from MAMBO-9. This tentative structure was thought to be related to a larger-scale $z \sim 6 \pm 0.2$ overdensity reported by M. Brinch et al. (2023), which may actually span multiple distinct substructures, connected by filaments (M. Brinch et al. 2024).

As is the case around HDF850.1, recent JWST/NIRSpec observations of the PRIMER-COSMOS field have greatly accelerated the confirmation of $z > 5$ galaxies. In addition to the spectrum of MAMBO-9-B presented in Section 3.4, we searched all spectra from CAPERS for objects potentially associated with MAMBO-9. We additionally searched DD#6585 (PI: D. Coulter), a Cycle 3 Director's Discretionary Time program targeting high-redshift supernova candidates, and GO#1810 (PI: S. Belli), a Cycle 1 program targeting massive galaxies at cosmic noon. Figure 9 shows the on-sky distribution of spectroscopically confirmed galaxies between z = 5.5 and 6.2 (colored by redshift), including Keck/VLT observations as well as JWST/NIRSpec. The inset panel shows the redshift histogram, revealing a clear excess of sources between z = 5.8–5.9, confirmed via their strong [O III] and/or Hα emission.

The structure appears to be quite large, spanning most of the PRIMER-COSMOS field, with 39 objects within $\Delta z = 0.03$ of MAMBO-9 (i.e., z = 5.82–5.88). While NIRSpec/MSA observations inherently suffer from incompleteness, NIRCam/WFSS observations, primarily from COSMOS-3D (GO#5893; PI: K. Kakiichi), will enable a more comprehensive mapping of the full protocluster and the filamentary structure as traced by Hα-emitters. If the structure indeed spans $\sim$40 cMpc, or is connected to another overdensity at $z \sim 6.0$ (M. Brinch et al. 2024), spanning line-of-sight distances $\sim$100 cMpc, it would be among the largest protoclusters known. Understanding how massive galaxies grow may require characterizing the environments they live in.

5. Summary

We have presented new high-resolution ALMA [C II] 158 μm and dust continuum observations and JWST/NIRCam+MIRI imaging of MAMBO-9, a merging pair of DSFGs at z = 5.85. We detect [C II] and dust continuum

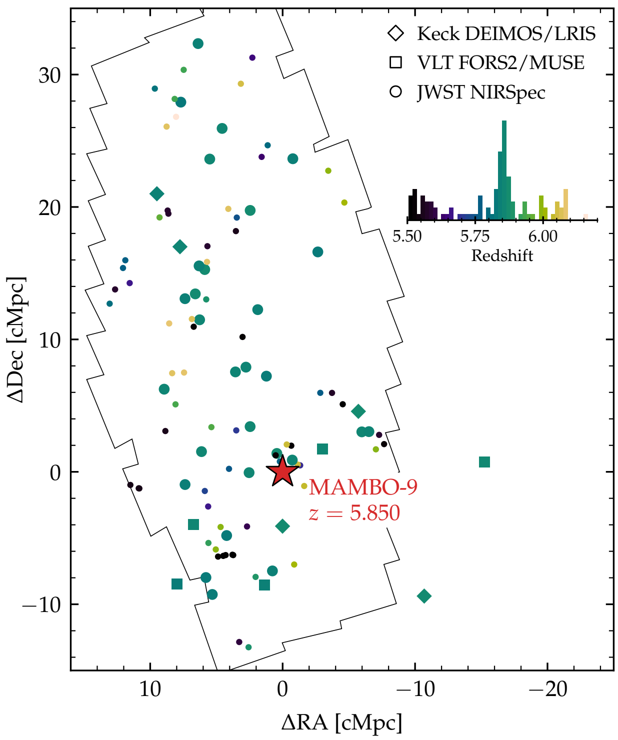

Figure 9. The overdense environment around MAMBO-9. We show objects spectroscopically confirmed in CAPERS between $z = 5.5$ and $z = 6.2$, while objects within $\Delta z = 0.03$ of MAMBO-9 are shown as larger points. We supplement this with 10 objects spectroscopically confirmed from ground-based Lyman-α surveys on Keck and VLT (G. Hasinger et al. 2018; L. Pentericci et al. 2018; K. B. Schmidt et al. 2021; B. Epinat et al. 2024), as compiled by A. A. Khostovan et al. (2026). The inset panel shows the redshift histogram, highlighting the clear excess of sources between $z = 5.8$ and 5.9. Note the large spatial scale of the structure, ~40 cMpc, spanning most of the PRIMER-COSMOS field.

emission in MAMBO-9-A and B. The dust continuum emission in both galaxies is concentrated in a central core, and MAMBO-9-B exhibits a tail toward MAMBO-9-A. The [C II] emission is more diffuse, and both galaxies exhibit [C II]/$L_{\rm FIR}$ ratios consistent with the "[C II] deficit," in which [C II] emission is weaker in region of higher FIR surface density. This trend holds in a spatially resolved analysis, indicating that the [C II] deficit arises from scales $\lesssim$400 pc.

Both galaxies exhibit double-peaked [C II] lines and clear velocity gradients, suggesting rotation. We fit the data cubes with $^{3\rm D}$BAROLO and derive dynamical masses of $(10.6 \pm 0.9) \times 10^{10}\,M_\odot$ for MAMBO-9-A and $(2.0 \pm 0.5) \times 10^{10}\,M_\odot$ for MAMBO-9-B. The mass ratio of ~1:5 is consistent with a minor merger.

New JWST/NIRCam+MIRI imaging reveals complex morphology in the rest-frame optical/NIR. MAMBO-9-A and B are connected by a continuous bridge, itself quite red, possibly a tidal tail from a recent interaction. The central cores of both galaxies, where the dust continuum emission peaks, are faint in the rest-frame optical. We conduct spatially resolved panchromatic SED fitting in 2D bins across the extent of the MAMBO-9 system; we find that while the bulk of the recent star formation is concentrated in compact, highly obscured ($A_V \gtrsim 10$) clouds, the bulk of the optical light is emergent from moderately obscured ($A_V \sim 1$–5) regions on the outskirts.

Comparison of the total baryonic mass ($M_\star + M_{\rm gas} + M_{\rm dust}$) to the derived dynamical masses requires a low $\alpha_{\rm CO}$ (~1–2) or GDR (~55–75), indicative of a highly metal-enriched ISM. MAMBO-9 appears to reside in a large overdensity: we identify 39 galaxies spectroscopically confirmed within ~25 cMpc of MAMBO-9, spanning most of the PRIMER-COSMOS field. Future spectroscopic efforts, including NIRCam WFSS observations from COSMOS-3D, will help reveal the connection between galaxy growth and environment.

Acknowledgments

H.B.A. acknowledges the support of the UT Austin Astronomy Department and the UT Austin College of Natural Sciences through the Harrington Graduate Fellowship, as well as the National Science Foundation for support through the NSF Graduate Research Fellowship Program. C.M.C. thanks the NSF for support through AST-2009577 and AST-2307006, as well as NASA through JWST-GO-01727. J.B.C. acknowledges funding from the JWST Arizona/Steward Postdoc in Early galaxies and Reionization (JASPER) Scholar contract at the University of Arizona. A.J.T. acknowledges support from the UT Austin College of Natural Sciences and from STScI/NASA through JWST-GO-6368. This paper makes use of the following ALMA data: ADS/JAO.ALMA#2021.1.00505.S. ALMA is a partnership of ESO (representing its member states), NSF (USA), and NINS (Japan), together with NRC (Canada), NSTC and ASIAA (Taiwan), and KASI (Republic of Korea), in cooperation with the Republic of Chile. The Joint ALMA Observatory is operated by ESO, AUI/NRAO, and NAOJ. The National Radio Astronomy Observatory is a facility of the National Science Foundation operated under cooperative agreement by Associated Universities, Inc.

This work is based on observations made with the NASA/ESA/CSA James Webb Space Telescope, obtained at the Space Telescope Science Institute, which is operated by the Association of Universities for Research in Astronomy, Incorporated, under NASA contract NAS5-03127. Support for program No. GO-6368 was provided through a grant from STScI under NASA contract NAS5-03127. The data were obtained from the Mikulski Archive for Space Telescopes (MAST) at the Space Telescope Science Institute. These observations can be accessed via doi:10.17909/e6ft-my94.

Authors from UT Austin acknowledge that they work at an institution that sits on indigenous land. The Tonkawa lived in central Texas, and the Comanche and Apache moved through this area. We pay our respects to all the American Indian and Indigenous Peoples and communities who have been or have become a part of these lands and territories in Texas.

ORCID iDs

Hollis B. Akins https://orcid.org/0000-0003-3596-8794
Caitlin M. Casey https://orcid.org/0000-0002-0930-6466
Jaclyn B. Champagne https://orcid.org/0000-0002-6184-9097
Olivia Cooper https://orcid.org/0000-0003-3881-1397
Maximilien Franco https://orcid.org/0000-0002-3560-8599
Kirsten K. Knudsen https://orcid.org/0000-0002-7821-8873
Anton M. Koekemoer https://orcid.org/0000-0002-6610-2048

Arianna S. Long https://orcid.org/0000-0002-7530-8857
Allison Man https://orcid.org/0000-0003-2475-124X
Sinclaire M. Manning https://orcid.org/0000-0003-0415-0121
Jed McKinney https://orcid.org/0000-0002-6149-8178
Jorge Zavala https://orcid.org/0000-0002-7051-1100
Pablo Arrabal Haro https://orcid.org/0000-0002-7959-8783
Mark Dickinson https://orcid.org/0000-0001-5414-5131
Vasily Kokorev https://orcid.org/0000-0002-5588-9156
Anthony J. Taylor https://orcid.org/0000-0003-1282-7454

References

Accurso, G., Saintonge, A., Catinella, B., et al. 2017, MNRAS, 470, 4750
Algera, H. S. B., Inami, H., Oesch, P. A., et al. 2023, MNRAS, 518, 6142
Algera, H. S. B., Rowland, L., Stefanon, M., et al. 2026, MNRAS, 545, staf1897
Aretxaga, I., Wilson, G. W., Aguilar, E., et al. 2011, MNRAS, 415, 3831
Bagley, M. B., Finkelstein, S. L., Koekemoer, A. M., et al. 2023, ApJL, 946, L12
Barrufet, L., Oesch, P. A., Marques-Chaves, R., et al. 2025, MNRAS, 537, 3453
Barrufet, L., Oesch, P. A., Weibel, A., et al. 2023, MNRAS, 522, 449
Bertoldi, F., Carilli, C., Aravena, M., et al. 2007, ApJS, 172, 132
Blain, A. W., Smail, I., Ivison, R. J., Kneib, J.-P., & Frayer, D. T. 2002, PhR, 369, 111
Boogaard, L. A., Bouwens, R. J., Riechers, D., et al. 2021, ApJ, 916, 12
Bothwell, M. S., Smail, I., Chapman, S. C., et al. 2013, MNRAS, 429, 3047
Bouwens, R. J., Smit, R., Schouws, S., et al. 2022, ApJ, 931, 160
Brinch, M., Greve, T. R., Sanders, D. B., et al. 2024, MNRAS, 527, 6591
Brinch, M., Greve, T. R., Weaver, J. R., et al. 2023, ApJ, 943, 153
Bushouse, H., Eisenhamer, J., Dencheva, N., et al. 2023, JWST Calibration Pipeline, Zenodo, doi:10.5281/zenodo.8380331
Calzetti, D., Armus, L., Bohlin, R. C., et al. 2000, ApJ, 533, 682
Carnall, A. C., McLure, R. J., Dunlop, J. S., & Davé, R. 2018, MNRAS, 480, 4379
Casey, C. M. 2012, MNRAS, 425, 3094
Casey, C. M. 2016, ApJ, 824, 36
Casey, C. M., Chen, C.-C., Cowie, L. L., et al. 2013, MNRAS, 436, 1919
Casey, C. M., Narayanan, D., & Cooray, A. 2014, PhR, 541, 45
Casey, C. M., Zavala, J. A., Aravena, M., et al. 2019, ApJ, 887, 55
Casey, C. M., Zavala, J. A., Manning, S. M., et al. 2021, ApJ, 923, 215
Chapman, S. C., Neri, R., Bertoldi, F., et al. 2008, ApJ, 689, 889
Chen, C.-C., Liao, C.-L., Smail, I., et al. 2022, ApJ, 929, 159
Cheng, Y., Giavalisco, M., Backhaus, B. E., et al. 2025, ApJ, 979, 71
Chiang, Y.-K., Overzier, R. A., Gebhardt, K., & Henriques, B. 2017, ApJL, 844, L23
Chworowsky, K., Finkelstein, S. L., Boylan-Kolchin, M., et al. 2024, AJ, 168, 113
Colina, L., Crespo Gómez, A., Álvarez-Márquez, J., et al. 2023, A&A, 673, L6
Conway, J. E., Cornwell, T. J., & Wilkinson, P. N. 1990, MNRAS, 246, 490
Cooper, O. R., Casey, C. M., Zavala, J. A., et al. 2022, ApJ, 930, 32
Cornwell, T. J. 2008, ISTSP, 2, 793
Crespo Gómez, A., Colina, L., Álvarez-Márquez, J., et al. 2024, A&A, 691, A325
da Cunha, E., Groves, B., Walter, F., et al. 2013, ApJ, 766, 13
Dannerbauer, H., Kurk, J. D., De Breuck, C., et al. 2014, A&A, 570, A55
De Looze, I., Cormier, D., Lebouteiller, V., et al. 2014, A&A, 568, A62
Decarli, R., Walter, F., Venemans, B. P., et al. 2018, ApJ, 854, 97
Di Teodoro, E. M., & Fraternali, F. 2015, MNRAS, 451, 3021
Díaz-Santos, T., Armus, L., Charmandaris, V., et al. 2017, ApJ, 846, 32
Donevski, D., Lapi, A., Małek, K., et al. 2020, A&A, 644, A144
Donnan, C. T., Dickinson, M., Taylor, A. J., et al. 2025, ApJ, 993, 224
Donnan, C. T., McLure, R. J., Dunlop, J. S., et al. 2024, MNRAS, 533, 3222
Downes, D., & Solomon, P. M. 1998, ApJ, 507, 615
Draine, B. T., & Li, A. 2007, ApJ, 657, 810
Drew, P. M., & Casey, C. M. 2022, ApJ, 930, 142
Eisenstein, D. J., Willott, C., Alberts, S., et al. 2026, ApJS, 283, 6
Eldridge, J. J., Stanway, E. R., Xiao, L., et al. 2017, PASA, 34, e058
Engel, H., Davies, R. I., Genzel, R., et al. 2011, ApJ, 729, 58
Epinat, B., Contini, T., Mercier, W., et al. 2024, A&A, 683, A205
Erwin, P. 2015, ApJ, 799, 226
Franco, M., Casey, C. M., Koekemoer, A. M., et al. 2026, ApJ, 999, 200
Fudamoto, Y., Oesch, P. A., Schouws, S., et al. 2021, Natur, 597, 489
Fujimoto, S., Finkelstein, S. L., Burgarella, D., et al. 2023, ApJ, 955, 130
Gaia Collaboration, Brown, A. G. A., Vallenari, A., et al. 2018, A&A, 616, A1
Gentile, F., Casey, C. M., Akins, H. B., et al. 2024, ApJL, 973, L2
Genzel, R., Tacconi, L. J., Gracia-Carpio, J., et al. 2010, MNRAS, 407, 2091
Grogin, N. A., Kocevski, D. D., Faber, S. M., et al. 2011, ApJS, 197, 35
Haas, M., Klaas, U., Müller, S. A. H., Chini, R., & Coulson, I. 2001, A&A, 367, L9
Harikane, Y., Ouchi, M., Inoue, A. K., et al. 2020, ApJ, 896, 93
Harish, S., Kartaltepe, J. S., Liu, D., et al. 2025, ApJ, 992, 45
Hashimoto, T., Inoue, A. K., Mawatari, K., et al. 2019, PASJ, 71, 71
Hasinger, G., Capak, P., Salvato, M., et al. 2018, ApJ, 858, 77
Herard-Demanche, T., Bouwens, R. J., Oesch, P. A., et al. 2025, MNRAS, 537, 788
Hodge, J. A., da Cunha, E., Kendrew, S., et al. 2025, ApJ, 978, 165
Hughes, D. H., Serjeant, S., Dunlop, J., et al. 1998, Natur, 394, 241
Hung, C.-L., Casey, C. M., Chiang, Y.-K., et al. 2016, ApJ, 826, 130
Ivison, R. J., Greve, T. R., Serjeant, S., et al. 2004, ApJS, 154, 124
Jiao, Q., Gao, Y., & Zhao, Y. 2021, MNRAS, 504, 2360
Jin, S., Daddi, E., Magdis, G. E., et al. 2019, ApJ, 887, 144
Jones, G. C., Bunker, A. J., Telikova, K., et al. 2025, MNRAS, 540, 3311
Jones, G. C., Vergani, D., Romano, M., et al. 2021, MNRAS, 507, 3540
Kamieneski, P. S., Frye, B. L., Windhorst, R. A., et al. 2024, ApJ, 973, 25
Kennicutt, R. C., & Evans, N. J. 2012, ARA&A, 50, 531
Kepley, A. A., Tsutsumi, T., Brogan, C. L., et al. 2020, PASP, 132, 024505
Khostovan, A. A., Kartaltepe, J. S., Salvato, M., et al. 2026, ApJS, 282, 6
Killi, M., Watson, D., Fujimoto, S., et al. 2023, MNRAS, 521, 2526
Koekemoer, A. M., Aussel, H., Calzetti, D., et al. 2007, ApJS, 172, 196
Koekemoer, A. M., Faber, S. M., Ferguson, H. C., et al. 2011, ApJS, 197, 36
Kohandel, M., Pallottini, A., Ferrara, A., et al. 2019, MNRAS, 487, 3007
Kokorev, V., Jin, S., Magdis, G. E., et al. 2023, ApJL, 945, L25
Kroupa, P. 2002, Sci, 295, 82
Kuiper, E., Hatch, N. A., Miley, G. K., et al. 2011, MNRAS, 415, 2245
Leja, J., Carnall, A. C., Johnson, B. D., Conroy, C., & Speagle, J. S. 2019, ApJ, 876, 3
Leśniewska, A., & Michałowski, M. J. 2019, A&A, 624, L13
Litke, K. C., Marrone, D. P., Aravena, M., et al. 2022, ApJ, 928, 179
Litke, K. C., Marrone, D. P., Aravena, M., et al. 2023, ApJ, 949, 87
Litke, K. C., Marrone, D. P., Spilker, J. S., et al. 2019, ApJ, 870, 80
Madau, P., & Dickinson, M. 2014, ARA&A, 52, 415
Madden, S. C., Cormier, D., Hony, S., et al. 2020, A&A, 643, A141
Manning, S. M., Casey, C. M., Zavala, J. A., et al. 2022, ApJ, 925, 23
Marrone, D. P., Spilker, J. S., Hayward, C. C., et al. 2018, Natur, 553, 51
McKinney, J., Manning, S. M., Cooper, O. R., et al. 2023, ApJ, 956, 72
McMullin, J. P., Waters, B., Schiebel, D., Young, W., & Golap, K. 2007, ASPC, 376, 127
Michałowski, M. J. 2015, A&A, 577, A80
Miller, T. B., Chapman, S. C., Aravena, M., et al. 2018, Natur, 556, 469
Miller, T. B., Hayward, C. C., Chapman, S. C., & Behroozi, P. S. 2015, MNRAS, 452, 878
Nelson, E., Brammer, G., Giménez-Arteaga, C., et al. 2024, ApJL, 976, L27
Oesch, P. A., Brammer, G., Naidu, R. P., et al. 2023, MNRAS, 525, 2864
Oke, J. B. 1974, ApJS, 27, 21
Oteo, I., Ivison, R. J., Dunne, L., et al. 2018, ApJ, 856, 72
Pentericci, L., Vanzella, E., Castellano, M., et al. 2018, A&A, 619, A147
Pérez-González, P. G., Barro, G., Annunziatella, M., et al. 2023, ApJL, 946, L16
Perna, M., Arribas, S., Lamperti, I., et al. 2024, A&A, 690, A171
Planck Collaboration, Aghanim, N., Akrami, Y., et al. 2020, A&A, 641, A6
Rémy-Ruyer, A., Madden, S. C., Galliano, F., et al. 2014, A&A, 563, A31
Riechers, D. A., Bradford, C. M., Clements, D. L., et al. 2013, Natur, 496, 329
Rizzo, F., Vegetti, S., Fraternali, F., Stacey, H. R., & Powell, D. 2021, MNRAS, 507, 3952
Rodighiero, G., Enia, A., Bisigello, L., et al. 2024, A&A, 691, A69
Rowland, L. E., Hodge, J., Bouwens, R., et al. 2024, MNRAS, 535, 2068
Salim, S., Boquien, M., & Lee, J. C. 2018, ApJ, 859, 11
Sanders, R. L., Shapley, A. E., Jones, T., et al. 2023, ApJ, 942, 24
Schmidt, K. B., Kerutt, J., Wisotzki, L., et al. 2021, A&A, 654, A80
Schouws, S., Bouwens, R., Smit, R., et al. 2023, ApJ, 954, 103
Scoville, N., Murchikova, L., Walter, F., et al. 2017, ApJ, 836, 66
Scoville, N., Sheth, K., Aussel, H., et al. 2016, ApJ, 820, 83
Sérsic, J. L. 1963, BAAA, 6, 41
Shimasaku, K., Ouchi, M., Okamura, S., et al. 2003, ApJL, 586, L111
Smit, R., Bouwens, R. J., Carniani, S., et al. 2018, Natur, 553, 178
Smolčić, V., Aravena, M., Navarrete, F., et al. 2012, A&A, 548, A4
Spilker, J. S., Marrone, D. P., Aravena, M., et al. 2016, ApJ, 826, 112

Suess, K. A., Kriek, M., Price, S. H., & Barro, G. 2021, ApJ, 915, 87
Sugahara, Y., Álvarez-Márquez, J., Hashimoto, T., et al. 2025, ApJ, 981, 135
Sun, F., Helton, J. M., Egami, E., et al. 2024, ApJ, 961, 69
Tacchella, S., Finkelstein, S. L., Bagley, M., et al. 2022, ApJ, 927, 170
Tacconi, L. J., Genzel, R., Smail, I., et al. 2008, ApJ, 680, 246
Talia, M., Cimatti, A., Giulietti, M., et al. 2021, ApJ, 909, 23
Taylor, A. J., Kokorev, V., Kocevski, D. D., et al. 2025, ApJL, 989, L7
Venemans, B. P., Kurk, J. D., Miley, G. K., et al. 2002, ApJL, 569, L11
Venemans, B. P., Röttgering, H. J. A., Miley, G. K., et al. 2005, A&A, 431, 793
Venemans, B. P., Röttgering, H. J. A., Miley, G. K., et al. 2007, A&A, 461, 823
Vincenzo, F., Matteucci, F., Belfiore, F., & Maiolino, R. 2016, MNRAS, 455, 4183
Walter, F., Decarli, R., Carilli, C., et al. 2012, Natur, 486, 233
Wang, R., Wagg, J., Carilli, C. L., et al. 2013, ApJ, 773, 44
Wang, T., Schreiber, C., Elbaz, D., et al. 2019, Natur, 572, 211
Williams, C. C., Alberts, S., Ji, Z., et al. 2024, ApJ, 968, 34
Williams, C. C., Labbe, I., Spilker, J., et al. 2019, ApJ, 884, 154
Witstok, J., Jones, G. C., Maiolino, R., Smit, R., & Schneider, R. 2023, MNRAS, 523, 3119
Wuyts, S., Förster Schreiber, N. M., Wisnioski, E., et al. 2016, ApJ, 831, 149
Xiao, M., Oesch, P. A., Elbaz, D., et al. 2024, Natur, 635, 311
Zavala, J. A. 2021, RNAAS, 5, 15
Zavala, J. A., Buat, V., Casey, C. M., et al. 2023, ApJL, 943, L9
Zavala, J. A., Casey, C. M., da Cunha, E., et al. 2018a, ApJ, 869, 71
Zavala, J. A., Casey, C. M., Manning, S. M., et al. 2021, ApJ, 909, 165
Zavala, J. A., Casey, C. M., Spilker, J., et al. 2022, ApJ, 933, 242
Zavala, J. A., Montaña, A., Hughes, D. H., et al. 2018b, NatAs, 2, 56